

---

## Geometric Corrections of PRISMA Hyperspectral Satellite Images for Forest Ecosystem Monitoring

**Auteur :** Miceli, Florence

**Promoteur(s) :** Jonard, François; Nascetti, Andrea

**Faculté :** Faculté des Sciences

**Diplôme :** Master en sciences géographiques, orientation géomatique, à finalité spécialisée en geodata-expert

**Année académique :** 2022-2023

**URI/URL :** <http://hdl.handle.net/2268.2/18625>

---

### *Avertissement à l'attention des usagers :*

*Tous les documents placés en accès ouvert sur le site le site MatheO sont protégés par le droit d'auteur. Conformément aux principes énoncés par la "Budapest Open Access Initiative"(BOAI, 2002), l'utilisateur du site peut lire, télécharger, copier, transmettre, imprimer, chercher ou faire un lien vers le texte intégral de ces documents, les disséquer pour les indexer, s'en servir de données pour un logiciel, ou s'en servir à toute autre fin légale (ou prévue par la réglementation relative au droit d'auteur). Toute utilisation du document à des fins commerciales est strictement interdite.*

*Par ailleurs, l'utilisateur s'engage à respecter les droits moraux de l'auteur, principalement le droit à l'intégrité de l'oeuvre et le droit de paternité et ce dans toute utilisation que l'utilisateur entreprend. Ainsi, à titre d'exemple, lorsqu'il reproduira un document par extrait ou dans son intégralité, l'utilisateur citera de manière complète les sources telles que mentionnées ci-dessus. Toute utilisation non explicitement autorisée ci-avant (telle que par exemple, la modification du document ou son résumé) nécessite l'autorisation préalable et expresse des auteurs ou de leurs ayants droit.*

---



Sciences Faculty  
Geography Departement

# Geometric Corrections of PRISMA Hyperspectral Satellite Images for Forest Ecosystem Monitoring

Master Thesis presented by : **MICELI Florence**

**Geographic Sciences, Geomatics Orientation, Geodata-Expert  
Finality**

Academic Year : **2022 - 2023**  
Defense Date : **September 2023**

Jury President : Prof. **René WARNANT**  
Promoter : Prof. **François JONARD**  
Co-promoter : Prof. **Andrea NASCETTI**  
Reading Jury : Prof. **Roland BILLEN,**  
Prof. **René WARNANT**



# Dedication

First, I would like to thank Pr. François Jonard and Pr. Andrea Nascetti for their unvaluable insights and encouragement during the research and writing of this master thesis.

I would also like to express my sincere appreciation to Marie Ebroin, Anthony Mungiovi, Julien Hutzemakers and my mum for their time in reading and providing valuable feedback on this thesis. Their comments and suggestions have greatly improved the quality of this work, and I am truly grateful for their support.

Furthermore, I would also like to extent my gratitude to my family for their support and encouragement throughout my academic journey. Their constant presence and support have given me the strength and motivation to overcome the challenges and obstacles that I have faced during my academic years.

Finally, I would like to thank my friends, with whom I have shared an incredible five-year journey at the university. Their presence has made this journey more meaningful and memorable, and I am truly grateful for their friendship and support.

# Résumé

La mission PRISMA est une mission spatiale hyperspectrale entièrement financée par l'Agence Spatiale Italienne. Cette mission scientifique et expérimentale a été lancée en 2019 et vise à fournir des images hyperspectrales à haute résolution à la communauté scientifique. Les études menées jusqu'à présent ont mis en évidence l'utilité de ces données mais très peu ont souligné leurs limites. Des écarts ont été identifiés sur les images hyperspectrales géocodées PRISMA lorsqu'elles sont comparées à des cartes de référence. Par conséquent, la précision de géolocalisation de ces images est remise en question. Ce mémoire vise à apporter des corrections géométriques aux images hyperspectrales PRISMA dans le but de fournir des images géolocalisées précises pour une surveillance exacte et fiable d'un écosystème forestier. Pour effectuer ces corrections, la méthode proposée implique un processus d'orthorectification qui repose sur l'utilisation de points de contrôle au sol. Les résultats ont montrés que la méthodologie proposée permettait d'améliorer la précision de géolocalisation de toutes les images hyperspectrales PRISMA. Il a également été observé qu'une amélioration de 166 m pouvait être atteinte, illustrant ainsi le potentiel de la méthodologie à être utilisée pour une surveillance précise d'un écosystème forestier.

# Abstract

The PRISMA mission is a spaceborne hyperspectral mission fully funded by the Italian Space Agency. This scientific and demonstrative mission launched in 2019 aims at providing high-resolution hyperspectral images to the research community. The studies conducted so far have highlighted the usefulness of the hyperspectral data delivered by this mission but very few have pointed out their limitations. Shifts have been identified in PRISMA geocoded hyperspectral images when compared to reference maps. Consequently, this raises question about the accuracy of the geolocation of these images. This master thesis aims at providing geometric corrections to the PRISMA hyperspectral images in the perspective of delivering accurately geolocated images for an accurate and reliable monitoring of forest ecosystem. To perform these corrections, the suggested method involves an orthorectification process that relies on the use of ground control points. The results showed that the suggested methodology allowed to increase the geolocation accuracy of all the PRISMA hyperspectral images and that improvement up to 166m can be achieved, which indicates the potential of the methodology to be used for accurate forest ecosystem monitoring.

# Contents

<b>1</b>	<b>Introduction</b>	<b>15</b>
<b>2</b>	<b>Overview of Hyperspectral Remote Sensing</b>	<b>16</b>
2.1	Principles of Hyperspectral Imaging . . . . .	16
2.1.1	Spectroscopy . . . . .	16
2.1.2	Imaging Spectroscopy . . . . .	16
2.1.3	Hyperspectral Remote Sensing . . . . .	18
2.1.4	Distinction between Hyperspectral and Multispectral Remote Sensing . .	19
2.2	Brief History of Hyperspectral Remote Sensing . . . . .	20
2.3	Hyperspectral Remote Sensing and Photochemical Reflectance Index . . . . .	21
<b>3</b>	<b>The PRISMA Italian Hyperspectral Mission</b>	<b>23</b>
3.1	PRISMA - The Italian Hyperspectral Mission . . . . .	23
3.2	Space Segment . . . . .	24
3.3	Ground Segment . . . . .	26
3.4	PRISMA Products . . . . .	26
3.4.1	Levels of PRISMA Products . . . . .	26
3.4.2	Level - 0 . . . . .	27
3.4.3	Level - 1 . . . . .	27
3.4.3.1	Product Generation Process . . . . .	27
3.4.3.2	Product Description . . . . .	28
3.4.4	Level - 2 . . . . .	29
3.4.4.1	Product Generation Process . . . . .	29

3.4.4.2	Product Description . . . . .	29
3.4.4.3	Level - 2B . . . . .	30
3.4.4.4	Level - 2C . . . . .	30
3.4.4.5	Level - 2D . . . . .	31
3.5	PRISMA Applications . . . . .	32
<b>4</b>	<b>Objective of the Master Thesis</b>	<b>35</b>
<b>5</b>	<b>Study Area and Dataset</b>	<b>37</b>
5.1	Area of Interest . . . . .	37
5.2	PRISMA Imagery . . . . .	38
5.3	Sentinel - 2 Imagery . . . . .	38
5.4	Digital Elevation Model . . . . .	39
<b>6</b>	<b>Methodology</b>	<b>40</b>
6.1	Proposed Methodology to Correct the PRISMA Hyperspectral Images . . . . .	40
6.2	Evaluation of the PRISMA Geocoded Hyperspectral Images . . . . .	43
6.3	Orthorectification Process . . . . .	46
6.3.1	Collection of Ground Control Points . . . . .	46
6.3.2	Rational Function Model . . . . .	47
6.3.2.1	Assessment of the Initial Rational Function Model . . . . .	48
6.3.2.2	Refinement of the Rational Function Model . . . . .	48
6.3.2.3	Assessment of the Refined Rational Function Model . . . . .	48
6.4	Evaluation of the Hyperspectral Images Orthorectified with the Proposed Methodology . . . . .	49
6.5	Assessment of the Orthorectification Process . . . . .	49
<b>7</b>	<b>Results</b>	<b>50</b>
7.1	Manual Collection of the Reference Points and the Ground Control Points . . . . .	50
7.2	Evaluation of the PRISMA Geocoded Hyperspectral Images . . . . .	50
7.2.1	Detected shifts . . . . .	50

7.2.2	Root Mean Square Errors . . . . .	51
7.2.3	Geolocation Accuracy . . . . .	52
7.3	Orthorectification . . . . .	52
7.3.1	Assessment of the Rational Function Models . . . . .	52
7.3.2	Assessment of the Refined Models . . . . .	53
7.4	Evaluation of the PRISMA Hyperspectral Images Orthorectified with the Proposed Methodology . . . . .	54
7.4.1	Detected Shifts . . . . .	54
7.4.2	Root Mean Square Errors . . . . .	55
7.4.3	Geolocation accuracy . . . . .	55
<b>8</b>	<b>Discussion</b>	<b>56</b>
8.1	PRISMA Geocoded Hyperspectral Images . . . . .	56
8.1.1	Shifts and Root Mean Square Errors Evaluation . . . . .	56
8.1.2	Geolocation accuracy . . . . .	57
8.2	Evaluation of the Refinement Process . . . . .	57
8.3	Evaluation of the Orthorectification Process . . . . .	58
<b>9</b>	<b>Conclusion</b>	<b>61</b>
<b>10</b>	<b>Future Perspectives</b>	<b>62</b>
<b>11</b>	<b>Appendixes</b>	<b>64</b>
11.1	Appendix 1 . . . . .	64
11.2	Appendix 2 . . . . .	65
11.3	Appendix 3 . . . . .	65
11.4	Appendix 4 . . . . .	66
11.5	Appendix 5 . . . . .	66
11.6	Appendix 6 . . . . .	67
11.7	Appendix 7 . . . . .	67
11.8	Appendix 8 . . . . .	67



# List of Figures

2.1	Three-dimension dataset of an imaging spectrometer (Garini <i>et al.</i> , 2006). . . . .	17
2.2	Illustration of the concept and principle of a hyperspectral satellite (Qian, 2021). . . . .	18
2.3	Overview of the spectral and spatial resolution of selected airborne and spaceborne hyperspectral and multispectral sensors (Guanter <i>et al.</i> , 2016). . . . .	19
3.1	Production chain of the Level - 1 products (ASI, 2021; modified). . . . .	27
3.2	Production chain of the Level - 2 products (ASI, 2021; modified). . . . .	29
5.1	Location of the Vielsam ICOS station. . . . .	37
6.1	Flowchart of the PRISMA orthorectification process. . . . .	41
6.2	Flowchart of the proposed methodology. . . . .	43
6.3	Location of the reference points. . . . .	44
6.4	Flowchart of the processing steps to compute the RMSE and CE90. . . . .	45
6.5	Location of the ground control points. . . . .	47
8.1	RMSE values for EnMAP L1C products in pixel (DLR, 2023). . . . .	59

# List of Tables

2.1	Overview of spaceborne hyperspectral imagers. . . . .	21
3.1	Main characteristics of PRISMA space segment (ASI, 2020;ASI, 2021). . . . .	25
3.2	PRISMA products (ASI, 2021). . . . .	26
3.3	Dimensions of the hyperspectral data of the L1 products (ASI, 2020). . . . .	28
3.4	Dimensions of the panchromatic data of the L1 products (ASI, 2020). . . . .	28
3.5	Geolocation accuracy of Level - 2 products (ASI, 2021). . . . .	30
5.1	PRISMA imagery acquired over the study area. . . . .	38
5.2	Characteristics of Sentinel - 2 Imagery . . . . .	38
6.1	List of the reference points. . . . .	43
6.2	List of the ground control points. . . . .	46
7.1	Coordinates shifts of the PRISMA geocoded hyperspectral images. . . . .	51
7.2	Root mean square errors on the North - East coordinates on the PRISMA geocoded hyperspectral images. . . . .	51
7.3	Geolocation accuracy of the PRISMA geocoded hyperspectral images. . . . .	52
7.4	Number of GCPs collected on each PRISMA hyperspectral images. . . . .	52
7.5	Standard deviation and mean of row and column residual errors of the initial rational function models. . . . .	53
7.6	Standard deviation and mean of row and column residual errors of the refined rational function models. . . . .	54
7.7	Coordinates shifts of the PRISMA hyperspectral images orthorectified with the suggested methodology. . . . .	54

7.8	Root mean square errors on the North - East coordinates on the PRISMA hyperspectral images orthorectified with the suggested methodology. . . . .	55
7.9	Geolocation accuracy of the PRISMA hyperspectral images orthorectified with the suggested methodology. . . . .	55
8.1	Differences between the absolute mean residual errors before and after the refinement process. . . . .	57
8.2	Maximum accuracy obtained by the rational polynomial function model on three test sites (Baiocchi <i>et al.</i> , 2022). . . . .	58

# Acronyms

Acronym	Meaning
AIS	Airborne Imaging Spectrometer
ASI	Italian Space Agency
CASI	Compact Airborne Spectrographic Imager
CE90	Circular error at 90% confidence
CHRIS	Compact High Resolution Imaging Spectrometer
CDD	Charge-Coupled Devices
CIBR	Continuum Interpolated Band Ratio
CNM	National Multimission Centre
CP	Check Point
DSI	Damaged Severity Index
DEM	Digital Elevation Model
EO	Earth Observing
ESA	European Space Agency
FDS	Flight Dynamics System
GCP	Ground Control Point
HypSEO	Hyperspectral Satellite for Earth Observation
ICU	Internal Calibration Unit
ICOS	Intergrated Carbon Observation System
JHM	Joint Hyperspectral Mission
JPL	Jet Propulsion Laboratory
L0	PRISMA Level – 0 product
L1	PRISMA Level – 1 product
L2	PRISMA Level – 2 product
L2B	PRISMA Level – 2B product
L2C	PRISMA Level – 2C product
L2D	PRISMA Level – 2D product
MCC	Mission Control Centre
NIR	Near-Infrared
PDHT	Payload Data Handling and Transmission subsystem
PFRS	Portable Field Reflectance Spectrometer
PRI	Photochemical Reflectance Index
RFM	Rational Function Model
RMSE	Root Mean Square Error
RPC	Rational Polynomial Coefficient
RPF	Rational Polynomial Function
SCC	Satellite Control Centre
SCS	Satellite Control System

STRM	Shuttle Radar Topography Mission
SWIR	Short-Infrared
TOA	Top of Atmosphere
TT&C	Tracking, Telemetry and Command station
VIS	Visible
VNIR	Visible and Near-Infrared

## Units

Abbreviation	Units
km	kilometers
m	meters
nm	nanometers

# Chapter 1

## Introduction

Hyperspectral imagery is an advanced tool that offers detailed information about the composition and characteristics of features. Numerous studies have emphasized about the richness and the benefits of hyperspectral data. Recent technological advancements have resulted in the development of advanced hyperspectral sensors such as DESIS, PRISMA, HISUI and EnMAP. These next generation spaceborne hyperspectral sensors enable to collect data with greater precision and spectral resolution thereby further arising opportunities in various applications.

Given the pressing need to monitor the impact of global warming on ecosystems, the richness of the hyperspectral data can be invaluable tool. Specifically, the detailed spectral information they offer can enable to estimate ecosystem health by tracking changes in photosynthetic activity over time. The photochemical reflectance index, which reveals stress patterns on leaf level, can be a useful indicator to track such changes. By using hyperspectral data to compute the index, which can only be computed with sufficiently narrow spectral bands, can allow mapping canopy stress in forest areas, and identify areas that may require further attention.

The latest hyperspectral data, such as the PRISMA data, can be used to compute the photochemical reflectance index. The PRISMA data are the products of the PRISMA mission, which is one of the latest spaceborne hyperspectral missions. Fully funded by the Italian Space Agency, the PRISMA satellite was launched on 22 March 2019 and has an expected operational lifetime of 5 years. This scientific and demonstrative mission aims at providing high-resolution hyperspectral images to the research community. Several studies have acknowledged the usefulness of these data in a variety of fields, which has broadly motivated the interest to exploit the latest spaceborne hyperspectral to evaluate canopy stress in forest areas. Mapping photosynthetic changes in forest areas over time with the latest hyperspectral data can enable better monitoring of such areas and highlights the benefits of using hyperspectral remote sensing to detect and monitor stress phenomena in forests.

The upcoming sections will provide an overview about hyperspectral remote sensing. Moreover, a presentation about the photochemical reflectance index and the PRISMA mission will be provided. The objectives of this master thesis will also be presented in greater detail.

## Chapter 2

# Overview of Hyperspectral Remote Sensing

### 2.1 Principles of Hyperspectral Imaging

#### 2.1.1 Spectroscopy

Spectroscopy be defined as the study of the absorption and emission of light and other radiation by matter (Chu *et al.*, 2023)

Materials reflect radiation differently across the electromagnetic spectrum when exposed to it. Indeed, the spectral response by a material as a function of the wavelength is unique and this is called its spectral signature. Such spectral measurements can be measured by devices such as spectrometers, spectrophotometers, spectrographs, and spectral analysers (Pu, 2017). Analyses of those measurements can enable for the detection and characterisation of materials. As a result, spectroscopy can be used in a wide range of fields including the remote sensing of the Earth.

#### 2.1.2 Imaging Spectroscopy

Also called hyperspectral imaging, imaging spectroscopy is the combination of spectroscopy and imaging. Imaging spectroscopy refers to the art and science of designing, evaluating, and applying instrumentation capable of simultaneously capturing spatial and spectral attributes of a scene with enough fidelity to preserve the fundamental spectral features that provide for object detection, classification, identification, and characterization (Eismann, 2012). Imaging spectroscopy can also be described as the acquisition of images where for each spatial resolution element in the image a spectrum of the energy arriving at the sensor is measured (*Imaging Spectroscopy*, n.d.).

Imaging spectrometers, which may also be known as hyperspectral imagers, capture both spatial and spectral information from each element within an image. These devices have the ability to acquired multiple wavelength ranges, commonly referred to as spectral bands, thereby enable the construction of a complete and continuous reflectance or radiance spectrum for every pixel in an image (Pu, 2017). To record spectral information, imaging spectrometers are equipped with an optical dispersing element which splits light into narrow, adjoining wavelength bands and the energy of each band is measured by a separate detector (Ortenberg, 2011).

In fact, the commonly used detectors in spectrometers are typically identified as Charged-Coupled Devices (CDD). Upon completing their data captures, imaging spectrometers generate a three-dimensional dataset referred to as a data cube. This dataset encompasses spatial (x,y) and spectral information ( $\lambda$ ) for every pixel found in an image. The data cube is depicted in figure 2.1, with X and Y coordinates representing the spatial dimensions and  $\lambda$  representing the spectral dimension. Thus, a data cube can be viewed as a collection of images acquired in narrow and contiguous spectral bands or a collection of many spectral values at each pixel (Garini *et al.*, 2006).

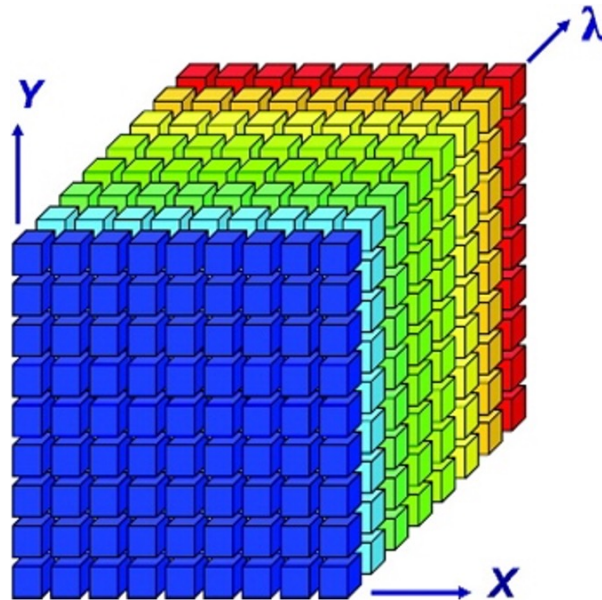


Figure 2.1 – Three-dimension dataset of an imaging spectrometer (Garini *et al.*, 2006).

Hyperspectral imagers are able to scan ground images through the use of two distinct scanning modes: whiskbroom and pushbroom. As a result, there are two methods for constructing data cubes from these scans. In the whiskbroom mode, a rotating scan mirror sweeps from one side to the other a scene and passes the radiations in the different wavelength ranges of every pixel in this scene onto the different elements of a CDD-linear array (Pu, 2017). Simultaneously, the imaging spectrometer platform moves in parallel with the motion of the mirror therefore leading to a sequential pixel-by-pixel and line-by-line scanning mode. Consequently, data cubes are built by sequentially recording one narrow image (one-pixel wide, multiple pixels long) swath after another with the corresponding spectral signature for each pixel in the swath. Pushbroom scanning mode uses a two-dimensional CDD-area array of detectors (Qian, 2021). The scanning mode is done in the along-track direction and one line is being scanned at a time without a rotating mirror. Therefore, data cubes are produced by the sequentially recording of one full spatial image after another, each at different wavelength (Pu, 2017). Pushbroom spectrometers have several advantages over their wishkbroom counterparts as they are lighter, smaller and have fewer moving parts (Ortenberg, 2011). Furthermore, this scanning has a high signal-to-noise ratio compared to the whiskbroom mode which has a low one (Pu, 2017). Nevertheless, pushbroom mode presents some drawback as much more detectors subject to calibration than the other scanning mode (Ortenberg, 2011).

### 2.1.3 Hyperspectral Remote Sensing

The ability of imaging spectrometers to be mounted on aircrafts and satellites has enabled the development of hyperspectral remote sensing. By relying on the imaging spectroscopy technique, this technology enables the collection of spectral information for each pixel in an image therefore offering another way of observing spatial phenomena on the surface of the Earth and in the atmosphere. The concept and principle of hyperspectral remote sensing are illustrated in the figure 2.2.

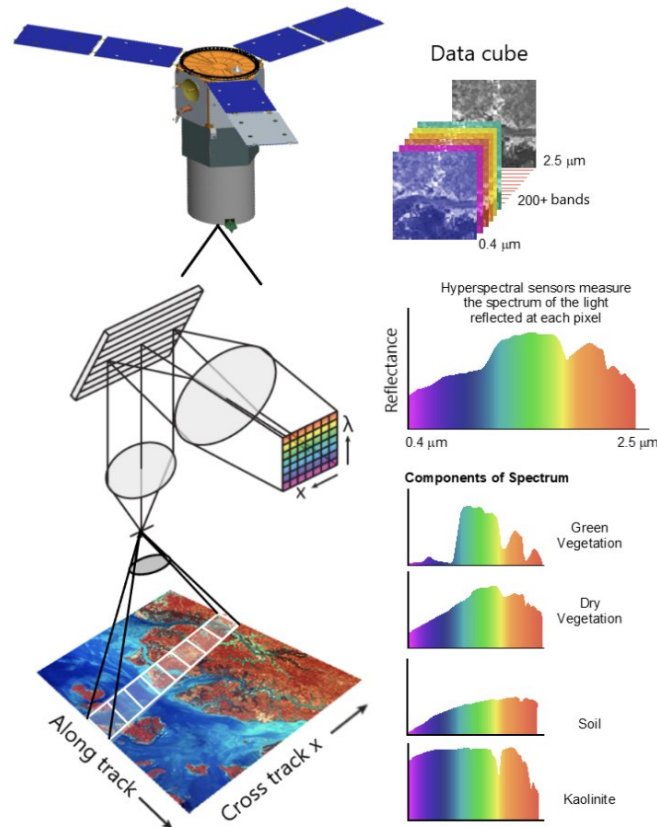


Figure 2.2 – Illustration of the concept and principle of a hyperspectral satellite (Qian, 2021).

A hyperspectral imager/sensor records hyperspectral images in narrow and continuous spectral bands usually ranging from the VIS to the SWIR region (380-2500 nm). As a result, the instrument generates a data cube composed of a series of images at different wavelengths. The spatial dimensions of this cube are determined by the cross-track and along-track directions of the imager. The along-track refers to the flight direction of the hyperspectral sensor platform whereas the cross-track refers to the perpendicular to this flight direction (Qian, 2021). The spectral dimension is determined by the complete and continuous range of radiance or reflectance values measured at each pixel.

The ability of hyperspectral sensors to acquire a complete and continuous radiance or reflectance spectrum enables the identification and characterisation of materials, and consequently the determination of their physical and chemical properties. The acquisition of subtle spectral information is essential for identifying the physical and chemical characteristics of materials and this can only be achieved by using a complete radiance or reflectance spectrum with a high spectral resolution.

As multispectral sensors only acquire data within a few broad spectral bands in certain wavelength ranges, they can not provide the same level of detailed information as hyperspectral sensors. Therefore, hyperspectral sensors can offer information which are not possible to acquire with the tradition remote sensing technologies such as multispectral. With such asset, hyperspectral imagery has been used up to now in various areas of interest such as minerals, water, vegetation, soils, ecosystems and the atmosphere (Pu, 2017).

### 2.1.4 Distinction between Hyperspectral and Multispectral Remote Sensing

The difference between hyperspectral and multispectral remote sensing lies in the acquisition of spectral bands. Hyperspectral sensors can acquire image data in dozens to a few hundred narrow and continuous spectral bands whereas in multispectral, sensors are able to acquire image data in a few wide and discrete spectral bands (Pu, 2017). The determining factor to be considered as a hyperspectral sensors is not the number of spectral bands but the spectral resolution. As a matter of fact, hyperspectral sensors have a finer spectral resolution than their multispectral counterparts. Figure 2.3 illustrates the spectral and spatial resolution of selected airborne and spaceborne hyperspectral and multispectral sensors, providing an overview of the different levels of spectral resolution offered by each type of sensor.

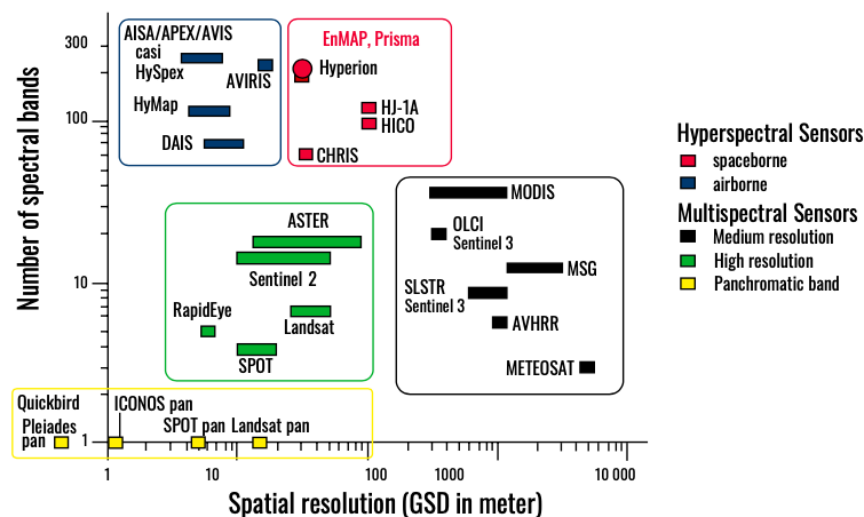


Figure 2.3 – Overview of the spectral and spatial resolution of selected airborne and spaceborne hyperspectral and multispectral sensors (Guanter *et al.*, 2016).

As previously mentioned, the great potential of hyperspectral remote sensing derives from its fine spectral resolution. The acquisition of numerous narrow and continuous spectral bands enables to have continuous spectral measurements across the electromagnetic spectrum, and therefore allowing to obtain much more spectral information.

## 2.2 Brief History of Hyperspectral Remote Sensing

The development of hyperspectral imaging, also known as imaging spectrometry, has expanded over the last decades and has emerged as a new generation of technology for earth observation.

Imaging spectrometry has emerged following the launch of the Landsat-1 satellite in 1972 (Pu, 2017). The Landsat multispectral scanner (MSS) recorded data in four wide spectral bands: green, red and infrared (Landsat 1, 2021). However, it was not able to discriminate minerals on the surface of the earth during data analysis due to its 100-200 nm wide spectral bands (Qian, 2021). To address this issue, the first portable field spectrometer, called the portable field reflectance spectrometer (PFRS), was developed in 1974 to cover spectral range from 400 to 2500 nm of the solar reflected radiance (Pu, 2017). The introduction of this field spectrometer has sparked a rise in interest in imaging spectrometry and has led to the developments of airborne hyperspectral imagers. In the early 1980s, the first airborne hyperspectral imager, known as the airborne imaging spectrometer (AIS), was developed (Qian, 2021). The AIS was a pushbroom hyperspectral imager using 2D detector arrays which contained 32 x 32 pixels (Pu, 2017). This spectrometer had the ability to acquire data spanning from 900 to 2100 nm (“tree mode”) to 1200 to 2400 nm (“rock mode”) wavelengths. The first images captured by the AIS were obtained in late 1982. These images are considered as the first hyperspectral images acquired onboard an aircraft (Pu, 2017). Since these images provided useful information to the scientific community, this technology had pursued its development and a second generation of the AIS (AIS-II) was built. The AIS-I flew from late 1982 to 1985 and the AIS-II flew from 1986 to 1987 (Pu, 2017). The AIS-II had a swath of 64 pixels whereas the first generation had only a swath of 32 pixels. The images from the second generation of the AIS had been widely used and had further arisen interest in hyperspectral remote sensing. Consequently, new airborne imaging spectrometers were designed by NASA with the help of the Jet Propulsion Laboratory (JPL). One of them was the Airborne Visible/Infrared Imaging Spectrometer (AVIRIS) whose development began in 1984. This whiskbroom sensor covered a spectral range from 400 to 2500 nm with a swath of 614 pixels. AVIRIS was first flown on board an aircraft in 1986 and was fully operational in 1989 (Qian, 2021). Since its development, this airborne imaging spectrometer has undergone modifications over the years especially in terms of spectral coverage and spatial resolution. In the late 1980s, the marketing of airborne hyperspectral imagers began with the Compact Airborne Spectrographic Imager (CASI) which was first introduced to the market in 1989 (Qian, 2021). The CASI has a total of 288 bands available, however the precise number could vary due to the ability to program the number of bands during flight. As a result, it became the first commercially programmable airborne hyperspectral imager. In the early 1990s, other airborne hyperspectral imagers were designed such as the Hyperspectral Digital Image Collection Experiment (HYDICE) in 1994 and the airborne hyperspectral mapper (HyMap) series.

The early 1990s were also marked by the launch of spaceborne hyperspectral imagers design. Regarded as the first spaceborne hyperspectral imager, Hyperion was launched in 2000 and was on board the NASA Earth Observing-1 (EO-1) satellite. This pushbroom hyperspectral imager contained 220 bands ranging from 400 to 2500 nm and had a 30-meter spatial resolution. Following the launch of Hyperion, the European Space Agency (ESA) launched its first spaceborne hyperspectral imager in 2001 on board the PROBA satellite. The Compact High Resolution Imaging Spectrometer (CHRIS) carried on board the ESA’s satellite covered the VIS and the NIR region: 400-1050 nm (Pu, 2017). However, the number of spaceborne hyperspectral imagers has significantly increased over time. In 2019, the PRISMA satellite was launched. Funded by the Italian Space Agency (ASI), this satellite offers high-spectral resolution hyperspectral data (ASI, 2020). The same year, the Hyperspectral Imager Suite (HISUI) was launched.

This spaceborne hyperspectral Earth imaging system was developed by the Japanese Ministry of Economy, Trade, and Industry (Japan Space Systems, n.d.). In 2022, the highly anticipated Environmental Mapping and Analysis Program (EnMAP) satellite was launched. This satellite is part of a German hyperspectral satellite mission with the aim to provide high-quality, region scale hyperspectral data for better understanding of environmental processes (DLR, n.d.).

In the future, additional hyperspectral data will be available with the upcoming launch of the Fluorescence Explored (FLEX) in 2024, the Spaceborne Hyperspectral Applicative Land and Ocean Mission (SHALOM) in 2025, and the Copernicus Hyperspectral Imaging Mission for the Environment (CHIME) in 2028. FLEX is an Earth observation mission which aims to provide detailed measurement of chlorophyll fluorescence from vegetation on land. This hyperspectral mission will be the first space mission to focus on the estimation of fluorescence emission on a global scale (ESA, 2017). Moreover, the SHALOM mission will provide high-resolution hyperspectral data at a 10-meter-spatial resolution. Furthermore, the CHIME mission will provide further hyperspectral data to support the monitoring, implementation, and improvement of a range of policies (ESA, 2020).

Table 2.1 provides an overview of past, present and future spaceborne hyperspectral imagers.

Sensor/ Mission	Launch	Spatial Resolution (m)	Number of Bands	Spectral Range (nm)	Spectral Resolution (nm)	References
Hyperion (U.S.A)	2000	30	220	400-2500	10	(Pu, 2017)
CHRIS (ESA)	2001	18-36	Up to 63	400-1050	1.5-11	(Pu, 2017)
MERIS (ESA)	2002	300	15	390-1040	1.8	(Pu, 2017)
GLI (Japan)	2002	250-1000	36	380-11950	10-1000	(Pu, 2017)
HySI (India)	2008	505.6	64	450-950	8	(Qian, 2021)
ARTEMIS (U.S.A)	2009	4	400	400-2500	5	(Pu, 2017)
VNIS (China)	2013	-	100	450-950	5	(Qian, 2021)
OLCI (ESA)	2016	300	520	390-1040	1.25	(Qian, 2021)
DESI (Germany)	2018	30	235	400-1000	2.55	(Qian, 2021)
PRISMA (Italy)	2019	30	239	400-1010	12	(ASI, 2021)
					920-2505	
HISUI (Japan)	2019	20	185	400-2500	10-12.5	(Japan Space Systems, nd.)
EnMAP (Germany)	2022	30	242	420-2450	6.5-10	(DLR, n.d.)
FLEX/FLORIS (ESA)	Planned in 2024	300	434	500-780	0.1 - 2	(ESA, 2017)
SHALOM (Italian - Israeli)	Planned in 2025	10	Unknown	400-2500	≤10nm	(Feingersh and Dor, 2015)
CHIME (ESA)	Planned in 2028	20-30	Over 200	400-2500	≤ 10 nm	(ESA, 2020)

Table 2.1 – Overview of spaceborne hyperspectral imagers.

## 2.3 Hyperspectral Remote Sensing and Photochemical Reflectance Index

Understanding vegetation health is an essential for its monitoring. There are several factors that can be used to evaluate this, such as the photosynthetic activity. One way to track changes in photosynthetic activity is by using the vegetation index called Photochemical Reflectance Index (PRI). The PRI is determined with the 531 and 570 nm reflectance wavelengths (Gamon *et al.*, 1992)<sup>1</sup>:

$$PRI = \frac{R_{531} - R_{570}}{R_{531} + R_{570}} \quad (2.1)$$

The PRI is a narrow-band index which is often calculated using hyperspectral data due to their ability to provide the high spectral resolution required for determining this index. This index measures the relative reflectance on either side of the green reflectance “hump” at 550nm (Garbulsky *et al.*, 2011; Sobhan, 2007).

1. R represents reflectance while the numbers indicate wavelength in nanometers.

As a matter of fact, this index encompasses the absorption wavelengths of chlorophylls and carotenoids (Garbulsky *et al.*, 2011). These plant pigments are essential components in photosynthesis since they absorb the light required for the process to take place. Furthermore, carotenoids are responsible for the protection of the photosynthetic machinery from damage due to excessive light exposure (Zulfiqar *et al.*, 2021). Consequently, the PRI can be referred to as an indicator of chlorophyll - carotenoid content. Overall, the index can serve as an indicator of chlorophyll - carotenoids ration and for both photosynthetic activity and vegetation health assessment due the importance of these pigments in the photosynthetic activity and their direction connection to this index.

This index has been used in various studies. For example, the PRI was used to assess the diurnal responses of photosynthesis to warming and drought (Zhang *et al.*, 2017). The results of this index was able to assess such changes in evergreen plants subjected to drought and warming conditions. The PRI can also been used for the detection of water stress in vegetation. A study focused on the evaluation of the effectiveness of this index for water stress detection in maize (Chou *et al.*, 2017). This study reported that the index, linked to chlorophyll and carotenoid pigments, showed a correlation with measured chlorophyll-carotenoid ratios at different water stress levels ( $R^2=0.58$ ). Furthermore, the study provided further explanation about the behavior of this index under water stress. As a matter, the study reported that under water stress, the carotenoid content increased while the chlorophyll content decreased, leading to a decrease in the chlorophyll-carotenoid radio and thereby to a decrease in the PRI value (Chou *et al.*, 2017). Moreover, the use of the PRI to be used as an indicator to study seasonal processes in forest areas. A study evaluated the response of the PRI to several ecohydrologic dynamics in a mixed conifer forest in the Coronado National Forest (Arizona, U.S.A). The outcomes of this results revealed that the PRI can be used as a proxy for plant response to ecohydrologic<sup>2</sup> variability of monsoon season in forest areas (Yang *et al.*, 2020). Another study investigated about the response of the PRI when wheat is subjected to elevated CO<sub>2</sub> and drought (Mulero *et al.*, 2023).

These studies are just few examples of how the PRI can be used with hyperspectral data to monitor changes in vegetation due to different stress factors like drought, heat, water stress, and elevates CO<sub>2</sub> levels. These studies assessed the impact of several stress factors on the PRI in order to better understanding how vegetation will response to environmental changes. Overall, computing this index will allow to detect how vegetation respond to changes in the environment over time.

---

2. Ecohydrology research investigates the effects of hydrological processes on the distribution, structure, and function of ecosystems, and on the effects of biotic processes on elements of the water cycle (Nuttle, 2021).

## Chapter 3

# The PRISMA Italian Hyperspectral Mission

### 3.1 PRISMA - The Italian Hyperspectral Mission

The PRISMA mission is an Italian Satellite Earth Observation hyperspectral mission led and fully funded by the Italian Space Agency (ASI) (Loizzo *et al.*, 2016). PRISMA (PREcursore IperSpettrale della Missione Applicative) was launched on 22nd March 2019 and has an expected operational lifetime of 5 years. The payload of the PRISMA satellite is composed of a hyperspectral spectrometer ranging from 400 to 2500 nm with a spatial resolution of 30m combined with a medium resolution panchromatic camera ranging from 400 to 700 nm with a spatial resolution of 5m (ASI, 2020).

The PRISMA mission is a follow-on of the discontinued Hyperspectral Satellite for Earth Observation (HypSEO) mission and the Joint Hyperspectral Mission (JHM) mission in collaboration with the Canadian Space Agency (ESA, 2012). The hyperspectral mission started in 2007 with the signature of the formal agreements between the Italian Space Agency and the contractor which consists of a consortium of Italian industries (Lopinto and Ananasso, 2013). The consortium is made up of industries that already have knowledge and experience in the development of satellites and panchromatic/hyperspectral sensors (ASI, 2009). Alongside the consortium of experienced industries, the scientific community and the future users were actively involved throughout the definition and development stages of the PRISMA mission. Specifically, the scientific community contributed to calibration and validation activities, algorithm definition, strategy formulation along with the research and development of applications that will exploit the hyperspectral data. Furthermore, the future users were involved in the definition of the mission specifications. As a result, the PRISMA mission is primarily focusing on meeting the requirements of Italian research and institutional entities. Beyond the definition and development phases, the scientific community is still involved in the mission as it is currently part of a program of scientific studies led by the ASI. The program is focused on researching specific products and applications while providing support to the mission in areas such as data processing algorithm evaluation, sensor calibration and independent verification of the system performances (Loizzo *et al.*, 2016).

The Italian hyperspectral mission is conceived as a pre-operative mission, aiming at qualifying the technology, developing new applications and providing products for institutional and scientific users for both environmental observation and risk management (Loizzo *et al.*, 2016). In addition, the mission is viewed as a scientific and demonstrative mission. The main objectives of the PRISMA mission are as follows (ASI, 2009):

- Implementation of an Earth Observation pre-operative mission.
- In orbit demonstration and qualification of an Italian state-of-the-art hyperspectral and panchromatic technology.
- Validation of end-to-end data processing able to develop new applications based on high spectral resolution images.
- Capitalisation of Italian Space Agency heritage, considering the HypSEO mission, the Italian-Canadian JHM study.

The overall objective of the mission is to provide institutional and research entities with high-resolution hyperspectral images of land, vegetation, inner waters, and coastal zone to support Earth Observation as well as the natural resource monitoring and management.

## 3.2 Space Segment

The PRISMA mission consists of a single satellite on a sun-synchronous Low Earth Orbit at 614.8km with a repeat cycle of approximately 29 days (Loizzo *et al.*, 2016). The PRISMA satellite<sup>1</sup> has a daily imaging capability of 200 00km<sup>2</sup> across an area of interest between 180°W-180°E and 70°S-70°N. The payload is composed of a high spectral resolution imaging spectrometer in the spectral range 400 - 2500 nm optically integrated with a medium resolution panchromatic camera in the spectral range 400 - 700 nm (Guarini *et al.*, 2018). Specifically, the hyperspectral instrument is composed of two imaging spectrometers. One is dedicated to the VNIR spectral range (400-1010nm) and the other is dedicated to the SWIR spectral range (920-2505nm). The panchromatic data are co-registered with the hyperspectral data to allow testing of image fusion techniques (ESA, 2012). At Nadir, the hyperspectral and panchromatic instruments have spatial resolutions of 30m and 5m, respectively. Based on a pushbroom technique, the satellite is able to collect images on areas of 30km swath width (Guarini *et al.*, 2018).

The table 3.1 presents the main features and properties of the PRISMA satellite.

The components of the satellite include the following elements:

- The platform.
- The payload.
- The Payload Data Handling and Transmission subsystem (PDHT).

The Payload is composed of the hyperspectral and panchromatic instruments and is responsible for the acquisition of hyperspectral and panchromatic images across the area of interest (180°W-180°E and 70°S-70°N). In addition to these instruments, the payload also contains an Internal Calibration Unit (ICU) which is responsible for the in-flight calibration. This unit allows operations of absolute and relative radiometric calibration as well as spectral calibration (Lopinto and Ananasso, 2013). The PDHT unit is responsible for storing the images collected by the sensors of the payloads in its internal memory. It is also in charge of transmitting these images to a ground station via a X-band link (ASI, 2021).

---

1. The mission and the satellite have the same name.

The PRISMA system can operate in a primary and a secondary mode. The primary mode refers to the collection of hyperspectral and panchromatic data of specific areas requested by end users. In other words, the acquisition of data by the satellite is driven by the user requests which can submit new image acquisition request on the PRISMA web portal. In the secondary mode, the satellite has an established ongoing ‘background’ task to acquire images in order to fully exploit the satellite resources (ASI, 2021). During an acquisition, the primary and the secondary modes can be used simultaneously or alternatively.

<b>PRISMA Orbit Characteristics</b>	
Orbit Altitude	614.8km
Inclination	98.19°
Nadir Revisit Time	29 days
Re-look Time	7 days
Local Time of Descending Node	10:30 AM
<b>PRISMA Satellite Main Characteristics</b>	
Swath	30km
FOV (Field of View)	2.77°
GSD (Ground Sampling Distance)	Hyperspectral : 30m Panchromatic : 5m
Spatial Pixels	Hyperspectral : 1000 Panchromatic : 6000
Pixel Size	Hyperspectral: 30x30 $\mu$ m Panchromatic : 6.5x6.5 $\mu$ m
Spectral Range	VNIR : 400-1010nm (66 bands) SWIR : 920-2505nm (173 bands) PAN : 400-700nm
SSI (Spectral Sampling Interval)	$\leq$ 12 nm
Spectral Width	$\leq$ 12 nm
Radiometric Quantisation	12 bit
SNR (Signal-to-Noise Ratio)	VNIR : > 200 : 1 SWIR : > 100 : 1 PAN : > 240 : 1
Absolute Radiometric Accuracy	Better than 5%

Table 3.1 – Main characteristics of PRISMA space segment (ASI, 2020;ASI, 2021).

### 3.3 Ground Segment

The PRISMA ground segment is composed of:

- The Satellite and Mission Control Centre.
- The Instrument Data Handling System (IDHS).

The Satellite and Mission Control centre is located in Fucino and is subdivided in the Satellite Control Centre (SCC) and the Mission Control Centre (MCC) subsystems. Within the ground segment, the MCC handles mission planning and management, while the SCC is responsible for the monitoring and the controlling of the satellite (Loizzo *et al.*, 2016). The SCC includes several subsystems, including the Satellite Control System (SCS), the Flight Dynamics System (FDS), and the Tracking, Telemetry and Command station (TT&C). Specifically, the FDS is supervising the orbit/ attitude operations and the TT&C is in charge of establishing and maintaining the two-way communication link between the satellite and the ground station through a S-band link (ASI, 2021). The IDHS is dedicated to the satellite data acquisition, processing, archiving and distribution. It is also responsible for the PRISMA users interfacing and support (Lopinto and Ananasso, 2013). The IDHS the PRISMA products by processing the hyperspectral data acquired via the X-band antenna of the National Multimission Centre (CNM) (Guarini *et al.*, 2018).

### 3.4 PRISMA Products

#### 3.4.1 Levels of PRISMA Products

The PRISMA mission delivers three levels of products to the users in the PRISMA web portal<sup>2</sup>. The different products available in the portal are listed in the table 3.2.

Level	Sub-Level	Description
Level-0 (L0)	/	Raw data stream including instrument and satellite ancillary data
Level-1 (L1)	/	Calibrated and coregistered Top of Atmosphere (TOA) radiance
Level-2 (L2)	Level-2B (L2B)	Geolocated at-ground spectral radiance
	Level-2C (L2C)	Geolocated at-surface reflectance
	Level-2C (L2D)	Geocoded at-surface reflectance

Table 3.2 – PRISMA products (ASI, 2021).

---

<sup>2</sup>. Registration is needed to have access to the PRISMA web portal. The portal can be accessed through the ASI website(<https://www.asi.it/scienze-della-terra/prisma/>).

### 3.4.2 Level - 0

The PRISMA Level – 0 products contain the following data:

- L0a Earth-Observation data (surface-observation file, surface-observation special file).
- L0a calibration data (dark calibration file, internal calibration file, internal calibration special file, sun calibration file, sun flux calibration file, moon-calibration file, and flat-field calibration file).
- Processing report file.
- Catalogue metadata files.

The Earth-Observation and calibration data files are saved in binary format. The processing report file describes is an XML file which describes the L0 processing execution. The catalogue metadata files are also in XML format and are available for each file included the L0 product (ASI, 2020).

### 3.4.3 Level - 1

#### 3.4.3.1 Product Generation Process

The processing chain to obtain the L1 product is outlined in the figure 3.1.

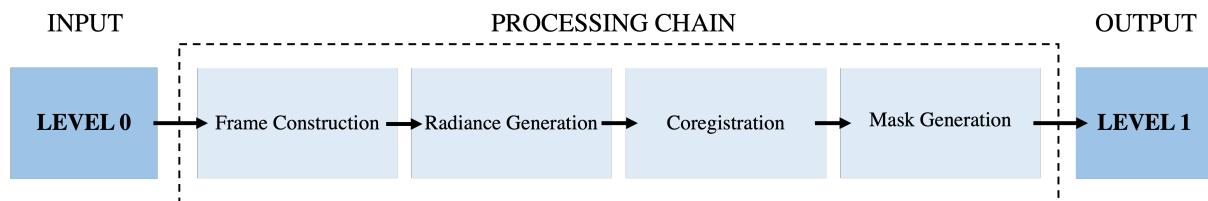


Figure 3.1 – Production chain of the Level - 1 products (ASI, 2021; modified).

The first processing step applied to the L0 product is frame construction. It transforms the L0a files contained in the L0 product into two lists of cubes, one for the VNIR/SWIR channel and the other for the panchromatic channel. The next step is radiance generation which converts the digital numbers of the L0a files to spectral radiances. The radiance cubes are then subjected to a coregistration process. Following the coregistration process, data masks such as cloud coverage, sun glint, and generic land covers are generated. The output of this processing chain is the PRISMA L1 product, which provides calibrated and registered Top of Atmosphere (TOA) radiance data.

### 3.4.3.2 Product Description

The PRISMA L1 files deliver calibrated and coregistered Top of Atmosphere (TOA) radiance data. This product level is stored as HDF5 files and contains the following layers of data:

- Radiometrically calibrated hyperspectral cube.
- Radiometrically calibrated coregistered hyperspectral cube.
- Radiometrically calibrated panchromatic image.
- Radiometrically calibrated coregistered panchromatic image.

The hyperspectral layers are arranged in a cube format, creating a three-dimensional dataset whose dimensions are presented in the table 3.3. The (X, Z) plane denotes as a monochromatic image whereas the (X, Y) denotes as a hyperspectral frame.

Axis	Description	Value
X	Spectral direction	66 bands for VNIR 173 bands for SWIR
Y	Along-track direction	1000 pixels
Z	Across-track direction	1000 pixels

Table 3.3 – Dimensions of the hyperspectral data of the L1 products (ASI, 2020).

The dimensions of the panchromatic images are presented in the table 3.4.

Axis	Description	Value
X	Along-track direction	6000 pixels
Y	Across-track direction	6000 pixels

Table 3.4 – Dimensions of the panchromatic data of the L1 products (ASI, 2020).

In addition to the four layers mentioned previously, the L1 product files also include data about the cloud coverage, sun glint and land cover masks. The cloud and sun glint masks highlight the pixels in an image that contain clouds or sun glint, while the land cover mask delivers a land cover map. Furthermore, the L1 product contains details regarding the processing conditions and the quality of the products. General information about the products is also archived in the L1 product files.

### 3.4.4 Level - 2

#### 3.4.4.1 Product Generation Process

The processing chain of the three L2 products is described in the figure 3.2. The first stage of the production of the L2 products is the atmospheric corrections. This process aims at removing the effect of atmospheric components from the measured TOA radiance. Specifically, this step aims at removing molecules and aerosols scattering as well as gaseous absorption. Following the implementation of the corrections, the geolocation process is initiated. This process updates the metadata section that refers to the geolocation of the input product and does not involve processing on the raster data (ASI, 2020). Subsequently, the water vapour and cloud optical thickness products as well as the aerosol optical thickness and Angstrom exponent product are generated. The water vapour product gives an insight of the moisture content, while the cloud optical thickness product delivers a measure of attenuation of the light passing through the atmosphere due to scattering and absorption by cloud droplets (SVS, 2013). After the generation of these products, further atmospheric corrections are applied to obtain the L2B product. Following additional processes including in particular a radiance-to-reflectance conversion step, the L2C product is produced. Once the conversion step is completed, the L2C product undergo an orthorectification process to generate the geocoded at-surface radiance L2D product. This process applied to the L2C product involves using auxiliary data, a Digital Elevation Model (DEM) as well as GCPs if available. As a result, the L2D product is an orthorectified at-surface radiance product projected on a cartographic UTM reference system.

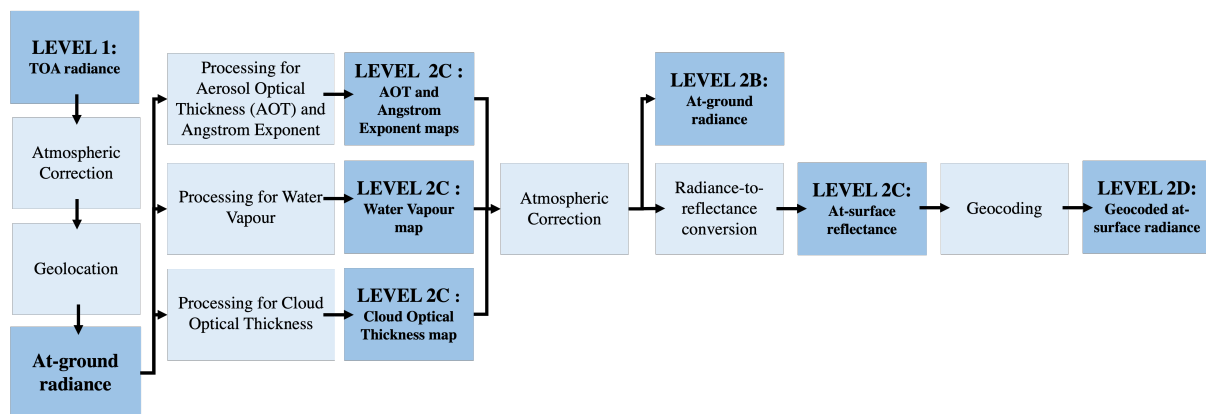


Figure 3.2 – Production chain of the Level - 2 products (ASI, 2021; modified).

#### 3.4.4.2 Product Description

The PRISMA Level – 2 has three types of products:

- Level – 2B: Geolocated at-ground spectral radiance product.
- Level – 2C: Geolocated at-surface reflectance product.
- Level – 2D: Geocoded at-surface reflectance product.

The hyperspectral layers of L2 products are arranged in a cube format and share the same dimensions as the L1 products. Furthermore, the panchromatic images have the identical dimensions to those in the L1 products.

The L2 products obtained from PRISMA are delivered with their corresponding orthorectification model (also called geocoding model) which which may be performed with or without the use of Ground Control Points (GCPs). The geolocation accuracy of the L2 products has been evaluated at five reference sites by the ASI and the resulting accuracy values are provided in the table 3.5 .

Parameter	CE90
Geolocation accuracy without GCPs	< 200m
Geolocation accuracy with GCPs	< 15m

Table 3.5 – Geolocation accuracy of Level - 2 products (ASI, 2021).

### 3.4.4.3 Level - 2B

The Level-2B product is a geolocated at-surface radiance product stored in the HDF5 format. The product consists of two layers:

- At-surface hyperspectral radiance cube.
- At-surface panchromatic radiance image.

Each layer included in the L2B product file has appended attributes such as the geographic localisation (latitude/longitude), the quality of the atmospheric correction applied, the GCPs and the orthorectification process attributes. The information related to GCPs in the L2B product is dependent on whether or not these points were used during the geolocation process. The orthorectification model is stored as a list of attributes for the hyperspectral and panchromatic layers but the model has not yet been applied at this level. Beyond these layers, the L2B product also contain information related to the product in general.

### 3.4.4.4 Level - 2C

The Level – 2C product provides geolocated at-surface reflectance data and maps related to atmospheric constituents. This product is formatted according to the HDF5 format and includes the layers that follow:

- At-surface hyperspectral reflectance cube.
- At-surface panchromatic reflectance image.
- Aerosol Optical Thickness map.
- Angstrom exponent map.
- Water Vapour map.
- Cloud Optical Thickness map.

Like the L2B product, the L2C product includes the geographic localisation, the quality of the atmospheric correction, the GCPs as well as the orthorectification model. As mentioned earlier, the section related to the GCPs is only available if these points were used during the geolocation process. Furthermore, general information about the product is also included in the L2C product files.

#### **3.4.4.5 Level - 2D**

The Level-2D product delivers geocoded surface reflectance data and encompasses the layers that follow:

- Geocoded surface reflectance hyperspectral cube .
- Geocoded surface reflectance panchromatic image.

The attributes available in the L2D product are the same to those found in previous levels. Nevertheless, the product also provides additional information about the orthorectification process.

### 3.5 PRISMA Applications

Since the availability of PRISMA data, several studies have been conducted to show their usefulness in several areas. In fact, PRISMA data can be used in a wide range of areas including soils, vegetation, agriculture, forestry, the atmosphere, coastal and inland waters, snow and ice as well as natural and anthropogenic hazards.

Several studies drew attention on the potential of the PRISMA hyperspectral data for vegetation traits retrieval. Tagliabue *et al.* (2022) developed a methodology for estimating leaf and canopy traits over an agricultural area in North-East Italy using PRISMA images collected in 2020 and 2021. Leaf and canopy level indices were obtained by using radiative transfer models that rely on PRISMA reflectance data. This study provides an insight of the usefulness of the hyperspectral data in the monitoring of vegetation over time. Another study investigated about the ability of these hyperspectral data to estimate topsoil properties over agricultural areas in Italy (Mzid *et al.*, 2022). The ability of the PRISMA data to approximate topsoil properties was assessed to compare the results of Landsat-8, Sentinel-2 data and field measurements. This study reported that soil property estimation models built with PRISMA resampled spectra have the most accurate estimations compared to multispectral and field data for the detection of clay, silt, sand, and organic carbon. As a matter of fact, the  $R^2$  coefficients were equal to 0.92, 0.90, 0.93 and 0.77, respectively (Mzid *et al.*, 2022). The results showed by this study hence encouraging the exploitation of imagery acquired by PRISMA for the quantitative estimation of soil properties. The spectral information contained in this sensor can also be used for the detection of non-photosynthetic vegetation (e.g. dead vegetation, surface plant litter and crop residues). A study, conducted over agricultural areas in Italy, reported that non-photosynthetic vegetation can be detected through the analysis of the behaviour of PRISMA reflectance spectra in the wavelength interval 2000-2200nm<sup>3</sup> (Pepe *et al.*, 2020). Furthermore, another recent study used PRISMA images for soil fertility mapping. Their research project focused on using PRISMA reflectance data for soil nutrients mapping over cultured area in Northern Morocco (Gasmi *et al.*, 2022). The study depicted that the values of the soil fertility maps created with PRISMA reflectance data were close to the measured values of soil nutrient contents over the study area. In addition, the PRISMA reflectance spectra showed similar behavior to the reflectance spectral obtained from soil samples analyses. Regarding the mapping of soil properties, another investigation evaluated the effectiveness of airborne HySpex<sup>4</sup> and spaceborne PRISMA hyperspectral data to map soil organic matter and carbonates (Angelopoulou *et al.*, 2023). According to this study, both hyperspectral sensors yielded comparable outcomes for the retrieval of soil organic matter over the study area in Northern Greece. However, the authors of this study suggested that further research should be carried out in order to improve carbonates estimation with PRISMA data. A recent study also employed PRISMA and Landsat-9 data for land use/land cover classification in a selected area in Turkey (Tuzcu Kokal *et al.*, 2022). The authors noted that the use of PRISMA images into classification models resulted in a slightly improvement in their accuracy. Specifically, the Landsat – 9 and PRISMA models achieved Kappa coefficient scores of 0.88 and 0.91, respectively. As a result of these findings, the classification models with PRISMA data were found to have a higher accuracy.

---

3. The 2000-2000nm spectral interval is referring to as the cellulose absorption band (Pepe *et al.*, 2020).

4. The HySpex sensor consists of two pushbroom hyperspectral cameras: HySpex VNIT-680 and HySpex SWIR-320. The sensor was created by the Norsk Elektro Optikk. The airborne hyperspectral sensor has a spectral range of 400-2500nm and a spectral sampling of 3.7nm for VNIR and 6.0nm for SWIR (Angelopoulou *et al.*, 2023).

Apart from the retrieval of crop traits, PRISMA hyperspectral data can be useful for forest types discriminations. A study found that PRISMA data outperform the Sentinel – 2 multispectral instrument in recognition of forest types (Vangi *et al.*, 2021). This study revealed that PRISMA data achieved a better discrimination of forest types due to their high spectral resolution. As a matter of fact, some forest types could only be differentiated through specific spectral ranges that were only by the PRISMA sensor.

The spectral information offered by the PRISMA hyperspectral sensor can also contribute to the management and monitoring of natural as well as anthropogenic hazards. The SAP4PRISMA<sup>5</sup> project, one of the five research projects funded by the Italian Space Agency, proposed a damage severity index (DSI) to assess the extent of damages on vegetated area (Bonis and Laneve, n.d.). Moreover, Seydi *et al.* (2021) conducted research about the usefulness of the PRISMA data in the detection of burned areas in Southern Australia. This study used pre-event and post-event data for predictions of burned areas. When Sentinel-2 data were used as pre-event data and PRISMA data as post-event data, an accuracy of 97.46 % was achieved over one study site in Southern Australia (compared to field measurements). However, an accuracy of 90.24% was achieved on the same study site when Sentinel-2 data were both used as pre- and post-event data. This study aimed to demonstrate the potential of PRISMA satellite images for accurate mapping of burned areas. Besides post-fire events, hyperspectral data can also be used for the characterisation of active fires. A research project evaluated PRISMA data for active wildfire detection during the Australian bushfires of 2019 in New South Wales (Amici and Piscini, 2021). The authors adapted three fire detection indices to PRISMA data to produce active fire detection maps. Two of the adapted indices obtained detection rates above 80% whereas the third index was reported as underperforming in comparison with the others. However, hyperspectral data demonstrated that they could offer accurate active fire predictions.

Recent studies also assessed PRISMA satellite data for water applications. For example, one research compared the TOA radiances from PRISMA L1 product with those from Sentinel-2 and a radiative transfer model (Giardino *et al.*, 2020). In this study, data were collected from various inland and coastal water across the globe. The comparison of the PRISMA radiances with the simulated radiances showed a  $R^2$  higher than 0.99 for all the investigated locations. In terms of comparing PRISMA with Sentinel – 2, the study reported a  $R^2$  value about 0.90 except at longer wavelengths where the correlation is weaker ( $R^2=0.589$  at 740nm). According to the authors, the decrease of the correlation might be explained by the fact that PRISMA data appeared to be slightly more scattered at longer wavelengths (Giardino *et al.*, 2020). Another research exploited the hyperspectral data from the PRISMA mission to map aquatic parameters in the aim of water quality monitoring (Bresciani *et al.*, 2022). Conducted over four lakes in Italy, the study presented some examples of water quality maps produced with the PRISMA data.

Beyond the applications already mentioned, PRISMA hyperspectral data can also be used for the retrieval of atmospheric constituents. A study drew attention on the potential of PRISMA data to be exploited for CO<sub>2</sub> emission retrieval at local scale. Romaniello *et al.* (2021) presented a methodology to retrieve CO<sub>2</sub> emission from PRISMA radiance data. It consisted of choosing the best PRISMA bands to compute the Continuum Interpolated Band Ratio (CIBR) index and then to convert the value of the index into CO<sub>2</sub> emission. One more study used PRISMA data to quantify methane emission over an industrial area in Turkmenistan (Nesme *et al.*, 2021). This research project investigated about the development of an approach to quantify CH<sub>4</sub> emission while using the radiance values from the PRISMA data.

---

5. SAP4PRISMA project has the objective of developing algorithms and products for supporting the PRISMA mission (Bonis and Laneve, n.d.)

The hyperspectral data from the PRISMA sensor can also be useful for cryosphere monitoring. A research investigated about the potentiality of the PRISMA images to retrieve snow properties in the Nansen Ice Shelf in East Antarctica (Kokhanovsky *et al.*, 2022). Snow properties were computed and then compared with values reported in the literature. Furthermore, another study focused on the use of PRISMA hyperspectral data for the retrieval of some ice and snow properties in the South-West Greenland ice sheet (Angelopoulou *et al.*, 2023). Ice and snow grains, ice and snow liquid water as well as glacier and snow algae were among the properties that have been retrieved during this study.

In addition to the studies focusing on the use of PRISMA data in various fields, several studies investigated about the radiometric performances of the PRISMA products. Indeed, a study compared the PRISMA radiance and reflectance values acquired over the Pignola site (Italian Southern Appenines) with modelled radiance and reflectance values obtained with field measurements (Pignatti *et al.*, 2022). The results indicated that there was a strong correlation between the PRISMA radiance values and the modelled radiance values as the  $R^2$  coefficient was above 0.98. With respect to reflectance values, a strong relationship was also observed until 2300nm. The study highlighted that the recognition of materials in wavelengths higher than 2300nm may cause issues for PRISMA L2C product. Another study also assessed the radiometric performances of the PRISMA products, acquired from July to August 2019, on the “Piazzo delle Concazze” on Mount Etna in Italy (Romaniello *et al.*, 2020). The study compared the PRISMA data with model simulations, data collected by the Hyperion sensor from 2001 to 2009, and field measurements acquired during field campaigns in July 2003. The outcomes of the comparisons revealed that PRISMA radiance and reflectance values were close to those from the model simulations, the Hyperion mission, and the field campaigns despite the difference in time acquisition between the datasets.

Overall, the usefulness of the PRISMA hyperspectral data have been acknowledged in many studies but very few highlighted the limitations of these data. Even though the PRISMA mission delivered geocoded hyperspectral images, shifts have been detected between the geocoded images and the references maps. A study depicted that a shift in all the PRISMA images was observed when compared to a reference map (Hamzeh *et al.*, 2023). This study mentioned that the images were geometrically correctly but did not specify the methodology used to achieve it. Another study also reported that a shift up to 5 pixels was observed in all PRISMA images (Mzid *et al.*, 2022). To geometrically correct the images, the authors resampled the images based on a reference grid using a Nearest Neighbour algorithm available in the ENVI software. This issue was also notified during the evaluation of the geometric correction capabilities of the PRISMA sensor over four years of operation (2019-2022). During this evaluation, it was reported that a shift of about 8 pixels in the longitudinal direction and 3 pixels in the latitudinal direction was observed between an image acquired in 2019 and one acquired in 2022 over the same study area (Pearlshtien *et al.*, 2023). Upon the above-mentioned studies, the methodologies used to correct the detected shifts have been briefly outlined. However, a study was entirely focused on the geometric correction of these displacements in the PRISMA panchromatic images (Baiocchi *et al.*, 2022). The suggested approach to achieve geometric correction of these images involves enhancing their orthorectification process applied to the images. To achieve this, some orthorectification techniques were experimented on the PRISMA panchromatic images.

## Chapter 4

# Objective of the Master Thesis

The previously studies have shown that PRISMA hyperspectral data are opening unprecedented opportunities in a wide range of areas including soils, vegetation, agriculture, forestry, the atmosphere, coastal and inland waters, snow, and ice as well as natural and anthropogenic hazards. This has broadly motivated the interest to exploit these data for estimating vegetation traits and more precisely for tracking changes on photosynthetic activity in a forest area in Belgium. As previously mentioned, the PRI has been identified as an indicator of such activity. Thus, the objective of this master thesis is to use PRISMA hyperspectral data to compute the PRI to keep track of changes in photosynthetic activity over a Belgian forest area.

The selection of the study area was based on the availability of PRISMA imagery near Integrated Carbon Observation System (ICOS) stations<sup>1</sup> in forest sites in Belgium. It was chosen to use PRISMA images near an ICOS station to assess the results of this work with field measurements obtained from this station. Following some on the PRISMA web portal, 7 PRISMA images were found to be available in Vielsam at a mixed forest type site. Specifically, geocoded at-surface reflectance data were retrieved which correspond to the PRISMA L2D products.

In order to obtain precise measurements of photosynthetic activity in the study area, it is essential to ensure that the used PRISMA hyperspectral images in the context of this work are accurately geolocated. The previous mentioned studies have pointed out that the PRISMA images may exhibit shifts despite being geocoded. Geolocation accuracy is crucial for accurate retrieving vegetation traits from PRISMA reflectance spectra. Inaccurate geolocation can result in measurements that do not correspond the actual ground conditions truth, leading to incorrect results. Therefore, this master thesis will also propose a methodology for geometrically correct the PRISMA hyperspectral images to obtain accurate and reliable results.

The objectives of this master thesis are therefore to firstly correct the geocoded PRISMA hyperspectral images to ensure accurate geolocation and then to track photosynthetic activity over the Vielsam ICOS with a focus on the PRI as indicator of this activity. However, the tracking of the photosynthetic activity using PRISMA geocoded hyperspectral images could not be accomplished due to technical limitations linked to the PRISMA products during their geometric corrections.

---

1. A ICOS station is a monitoring station which is part of the ICOS station network. This network is a European research infrastructure with the mission to produce standardised, high-precision and long-term observations and facilitate research to understand the carbon cycle and to provide necessary information on greenhouse gases (The ICOS Station Network, n.d.). ICOS stations within the network can measure greenhouse concentrations in the atmosphere, meteorological parameters as well as other environmental variables.

Therefore, this master thesis will be focusing on developing a methodology to correct the PRISMA hyperspectral images as a first step towards providing accurate geolocated hyperspectral images for the monitoring of a forest area.

The methodology to correct these images will be presented in the following sections. The next section will focus on introducing the study area and the data used in the context of this work. Following this, a detailed presentation of the methodology used to correct the PRISMA hyperspectral images will be available. The outcomes obtained using this approach will be presented and discussed. Finally, the work will be concluded by summarising the results of the proposed methodology and discussing about the potential uses of the corrected PRISMA hyperspectral images including their use to monitor photosynthetic activity over a forest area.

# Chapter 5

## Study Area and Dataset

### 5.1 Area of Interest

The area of interest in the scope of this work centers around the forest area surrounding the Vielsam ICOS station. Due to the availability of PRISMA imagery near this station, this has become the study area. A presentation of the location of the ICOS station is available in the figure 5.1.

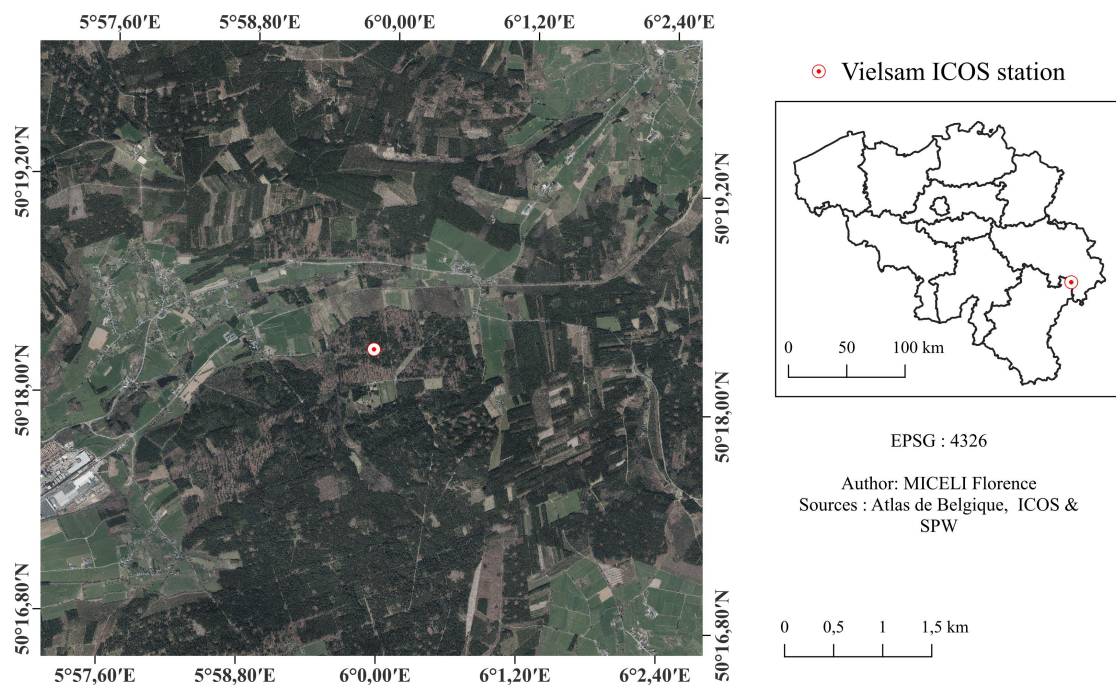


Figure 5.1 – Location of the Vielsam ICOS station.

## 5.2 PRISMA Imagery

Seven images have been obtained over the area of interest since the PRISMA satellite was launched. These images were captured between April 2020 and November 2023.

Since the launch of the PRISMA satellite, seven images are available over the area of interest. These images were captured between April 2020 and November 2022. Each hyperspectral image a have been downloaded on the PRISMA web portal at different processing levels: L1, L2B, L2C and L2D. The different hyperspectral images used in the context of this work are described in table 5.1.

ID of Hyperspectral Image	Acquisition Date	Cloud Coverage (%)	Acquisition start time	Acquisition stop time
1	20 April 2020	0.035	10:49:16	10:49:20
2	29 June 2020	25.059	10:55:38	10:55:42
3	27 February 2021	0.742	10:44:03	10:44:08
4	15 April 2022	3.013	10:49:20	10:49:25
5	5 July 2022	7.895	10:46:10	10:46:14
6	30 September 2022	7.380	10:46:03	10:46:07
7	10 November 2022	13.003	10:52:49	10:52:54

Table 5.1 – PRISMA imagery acquired over the study area.

The acquired PRISMA hyperspectral images have a spatial resolution of 30m and a cover area of 30 x 30km. Each image includes 239 bands ranging from the VNIR to the SWIR spectral regions, which span from 400 - 2505nm. Specifically, 66 bands are available for the VNIR spectral region and 173 bands for the SWIR spectral region.

To compute vegetation indices, such as the PRI, it is necessary to use at-surface reflectance data. Therefore, the focus of this work will be on using L2C (at-surface reflectance) and L2D (geocoded at-surface reflectance) from the PRISMA hyperspectral imagery.

## 5.3 Sentinel - 2 Imagery

As mentioned earlier, there is a possibility of shift in the PRISMA geocoded images. To determine whether this issue is present in the collected images, it is necessary to have a reference map. In the context of this work, the global and cloudless Sentinel – 2 map from 2021 will be used as the reference map. The Sentinel - 2 can be a useful tool for evaluating the geolocation accuracy of the geocoded PRISMA images, as it provides a 2m spatial resolution, cloud free view of the surface of the Earth (table 5.2 ). This map was obtained using the QGIS software and the QuickMapServices plugin.

<b>Name</b>	Sentinel-2 cloudless 2021 by EOX
<b>Spatial Resolution</b>	2m
<b>CRS</b>	EPSG:3857
<b>Last Update</b>	2 June 2022

Table 5.2 – Characteristics of Sentinel - 2 Imagery

## 5.4 Digital Elevation Model

Digital elevation models were also used in this work. These models are used to retrieve the elevation of the GCPs that will be used to correct the PRISMA hyperspectral images. The 30-meter-resolution Shuttle Radar Topography Mission (SRTM) data were used. Specifically, the N50EO05 and N50E006 data tiles were used<sup>1</sup>.

---

1. <https://dwtkns.com/srtm30m/>

# Chapter 6

## Methodology

### 6.1 Proposed Methodology to Correct the PRISMA Hyperspectral Images

To correct the PRISMA hyperspectral images, two solutions were proposed. The first one involved applying a translation process to the PRISMA L2D geocoded hyperspectral images. The second solution suggested making adjustments to the orthorectification process and subsequently applying this adjusted process on the PRISMA L2C hyperspectral images. Following some discussion, it was decided to implement the second solution. Accordingly, the PRISMA hyperspectral images will be corrected by proposing an alternative approach to orthorectify them than the one currently proposed. Orthorectification aims to geometrically correct an image to remove relief distortions, sensor artifacts, earth curvature and other perspectives distortions, and to align the image with coordinates on the ground (*Orthorectification*, n.d.). Thus, this process includes the orientation of the images and their projection onto a cartographic reference system. The orthorectification process currently being applied to the PRISMA Level-2 products (hyperspectral and panchromatic images)<sup>1</sup> can be described as shown in the figure 6.1.

Upon the completion of the process, the PRISMA Level – 2 processor delivers an orthorectified image that is projected onto a cartographic UTM reference system. The L2D panchromatic and hyperspectral images coordinates are specified in units of pixels, whereas the ground coordinates are given in decimal degrees of latitude and longitude. The images are referenced according to the WGS-84 reference system. Furthermore, the geodetic elevation is given in units of meters. It is worth to mention that the orthorectification process is only applied to the L2D products and is appended as metadata information to the L2B and L2C products.

The figure 6.1 indicates that the PRISMA products undergo orthorectification using a Rational Function Model (RFM) approach. This orthorectification approach uses polynomial ratios to link ground coordinates to their corresponding image pixel coordinates (Zhou *et al.*, 2018). In other words, the model associates the ground coordinates (latitude, longitude, and elevation) of specific points to their corresponding images coordinates (row, column). By coupling ground coordinates to image coordinates, the model allows for the correction of perspective distortions and terrain relief as well as georeferentiation.

---

1. Both the hyperspectral and panchromatic images are subjected to the same orthorectification process, but there are some variations in the steps taken for each type of image.

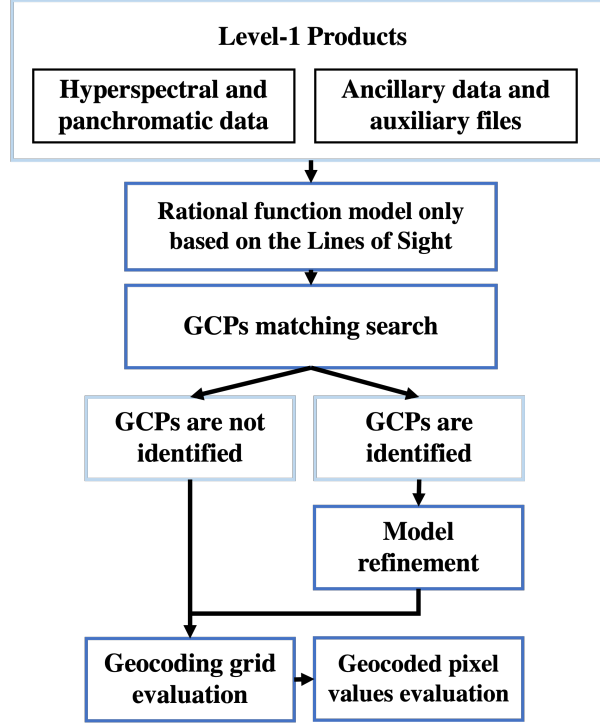


Figure 6.1 – Flowchart of the PRISMA orthorectification process.

For an individual PRISMA image, the ratios of the polynomials are expressed as:

$$r_n = \frac{p_A(X_n, Y_n, X_n)}{p_B(X_n, Y_n, X_n)} = \frac{\sum_{i=0}^3 \sum_{j=0}^3 \sum_{k=0}^3 a_{ijk} X_n^i Y_n^j Z_n^k}{\sum_{i=0}^3 \sum_{j=0}^3 \sum_{k=0}^3 b_{ijk} X_n^i Y_n^j Z_n^k} \quad (6.1)$$

$$c_n = \frac{p_C(X_n, Y_n, X_n)}{p_D(X_n, Y_n, X_n)} = \frac{\sum_{i=0}^3 \sum_{j=0}^3 \sum_{k=0}^3 d_{ijk} X_n^i Y_n^j Z_n^k}{\sum_{i=0}^3 \sum_{j=0}^3 \sum_{k=0}^3 d_{ijk} X_n^i Y_n^j Z_n^k} \quad (6.2)$$

Where  $(r_n, c_n)$  are the normalized row and column index of pixels in image space;  $(X_n, Y_n, Z_n)$  are the normalized longitude, latitude, and elevation of object points in ground space;  $a_{ijk}, b_{ijk}, c_{ijk}, d_{ijk}$  are the rational polynomial coefficients (RPC);  $p_A, p_B, p_D, p_D$  are the third-degree polynomials (ASI, 2021).

Specifically, one polynomial can be expanded as<sup>2</sup>:

$$\begin{aligned}
 p_A(X_n, Y_n, X_n) = & a_0 + a_1 \times X + a_2 \times Y + a_3 \times Z \\
 & + a_4 \times XY + a_5 \times XZ + a_6 \times YZ + a_7 \times X^2 \\
 & + a_8 \times Y^2 + a_9 \times Z^2 + a_{10} \times XYZ + a_{11} \times X^3 \\
 & + a_{12} \times XY^2 + a_{13} \times XZ^2 + a_{14} \times X^2Y + a_{15} \times Y^3 \\
 & + a_{16} \times YZ^2 + a_{17} \times X^2Z + a_{18} \times Y^2Z + a_{19} \times Z^3
 \end{aligned} \quad (6.3)$$

2. (ASI, 2021).

Considering the above formulas, normalized coordinates are used in the polynomial ratios. The use of normalized coordinates is necessary as it allows to reduce errors during the model computation (ASI, 2021). To achieve the normalization process, scale factors (S) as well as offsets (O) are applied to the ground coordinates. The coordinates are then normalized according to equations 6.4, 6.5 and 6.6.

$$X_n = \frac{X - X_0}{X_S} \quad (6.4)$$

$$Y_n = \frac{Y - Y_0}{Y_S} \quad (6.5)$$

$$Z_n = \frac{Z - Z_0}{Z_S} \quad (6.6)$$

Following the normalization of the ground coordinates, the image coordinates are normalized according to the equations 6.1 and 6.2 using the RPC provided in the PRISMA L2C products.

In general, the rational function model is solved by estimating the RPCs with a least-square process. Within the context of the PRISMA mission, the model appended to the L2B and L2C products supplies the coefficients and the parameters for normalizing the row, column, latitude, longitude and ellipsoidal height values (Baiocchi *et al.*, 2022). As a matter of fact, the model is computed based only on the Lines of Sight (LoS) information<sup>3</sup> read from the L1 products, and it does not rely on the use of a DEM or GCPs (ASI, 2021). As this model relies solely on the LoS information, it can suffer from a lack of accuracy (ASI, 2021). To address this issue, the Level-2 processor can enhance the accuracy of the model by using GCPs. However, it may not be possible to obtain GCPs for all PRISMA images due to limitations of the automatic GCPs matching procedure developed in the context of this Italian hyperspectral mission. In other words, such points may not be available for all images since the matching procedure can be unsuccessful. Consequently, the availability of GCPs has a significant impact on the geolocation accuracy of the PRISMA products. Indeed, the use of GCPs during the orthorectification process leads to a CE90 geolocation accuracy of less than 15m, whereas without their use a CE90 geolocation accuracy of less than 200m is obtained (ASI, 2021). As a result, using GCPs is essential to the enhancement of the geolocation accuracy of the PRISMA products. Consequently, it was proposed to collect manually GCPs on each L2C hyperspectral image and to use them to refine the rational function model of each image.

In the PRISMA processing context, the L2C products are orthorectified, resulting in the creation of L2D products that represent the geocoded versions of the L2C products. The methodology being proposed will use the same approach except that GCPs will be used to refine the rational function model. As a result, the methodology will deliver alternative versions of the PRISMA L2D hyperspectral products. It is worth mentioning that only the hyperspectral images will be orthorectified. The proposed methodology in the scope of this work can be summarised as the flowchart in the figure 6.2.

---

3. The sensor Line of Sight (LoS) describes how a point on the ground is projected onto the pixel in a satellite image (ASI, 2021).

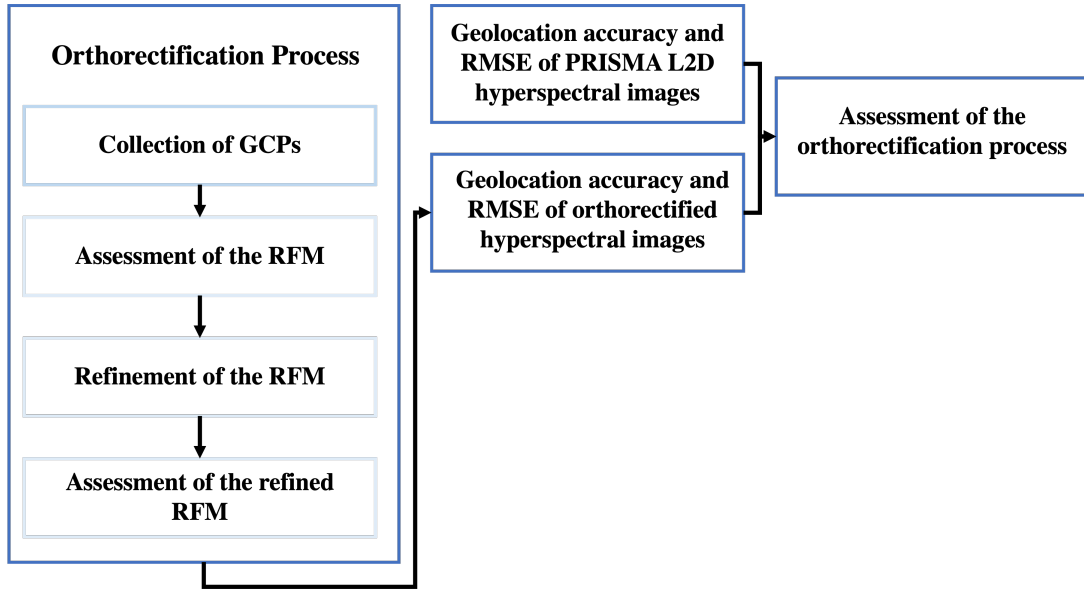


Figure 6.2 – Flowchart of the proposed methodology.

## 6.2 Evaluation of the PRISMA Geocoded Hyperspectral Images

Considering that some studies highlighted that shifts can be detected between PRISMA geocoded hyperspectral images and correctly georeferenced maps, it could be useful to detect the potential ones and to estimate them. By doing so, it will also be possible to calculate the geolocation accuracy of the geocoded hyperspectral images. Furthermore, the effectiveness of the orthorectification process of the PRISMA products can be determined.

Estimating the shifts involves comparing the coordinates of points in the PRISMA geocoded hyperspectral images and their corresponding coordinates on the Sentinel – 2 map. To achieve this, reference points were collected. In the context of this work, 5 reference points were selected on each hyperspectral image. These points were selected by considering that they must be different from the points that will be used for the refinement of the RFM. Furthermore, these points were selected by considering that they must be homogeneously distributed across the area delimited by the PRISMA hyperspectral images. Following these criteria, a total of 5 reference points were manually collected on both the reference map and the hyperspectral images using the EnMAP – Box plugin and the QGIS software.

The table 6.1 lists the 5 reference points collected in each hyperspectral image.

ID of Hyperspectral Image	ID of Reference Points
1	1,2,3,4,5
2	1,4,6,7,8
3	2,4,6,9, 10
4	4,11,12,13,14
5	1,4,15,16,17
6	2,17,18,19,20
7	5,10,21,22,

Table 6.1 – List of the reference points.

The figure 6.3 presents the reference points collected on the Sentinel – 2 reference map (EPSG:4326) and the PRISMA geocoded hyperspectral images.

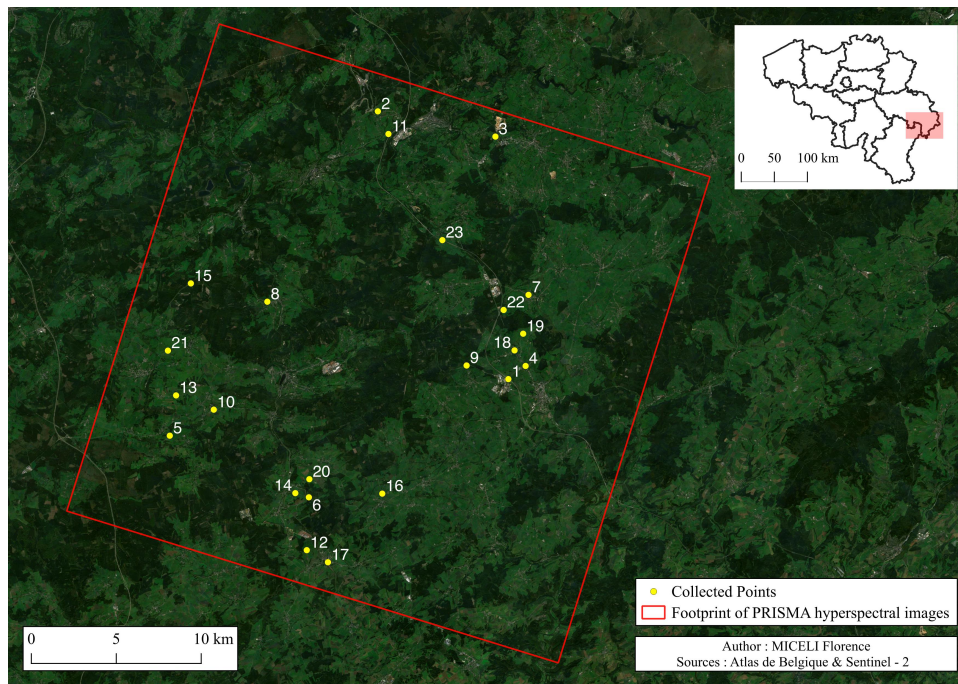


Figure 6.3 – Location of the reference points.

Once the reference points were collected on the QGIS software and the EnMAP – Box plugin, their North – East coordinates were retrieved in the WGS84 reference system<sup>4</sup>. Specifically, the coordinates were retrieved in meters using the UTM zone 31N and UTM zone 32N coordinates reference system according to the WGS84 datum (EPSG:32631 and EPSG:32632, respectively)<sup>5</sup>. Afterwards, the shifts can be estimated by computing the difference between the GCPs coordinates collected on the PRISMA geocoded hyperspectral images and the Sentinel – 2 reference map. The North and East shifts are computed based on the equations 6.7 and 6.8, respectively.

$$\Delta N(m) = PRISMA \text{ North coordinate}(m) - Sentinel - 2 \text{ North coordinate}(m) \quad (6.7)$$

$$\Delta E(m) = PRISMA \text{ East coordinate}(m) - Sentinel - 2 \text{ East coordinate}(m) \quad (6.8)$$

Following this, the Root Mean Square Error can be determined. This measure is the square root of the mean of the difference between the estimated coordinates and the actual coordinates. Computing the RMSE on the East and North coordinates will allow to compute the error on each coordinate (eq. 6.9 and eq. 6.10).

4. The EnMAP-Box plugin allowed to visualise the L2D hyperspectral images on the QGIS software.

5. The coordinates were retrieved in these reference systems because they are the systems according to which the PRISMA hyperspectral images are geocoded.

$$North - RMSE(m) = \sqrt{\frac{1}{n} \sum_{i=1}^n (\Delta N_i^2)} \quad (6.9)$$

$$East - RMSE(m) = \sqrt{\frac{1}{n} \sum_{i=1}^n (\Delta E_i^2)} \quad (6.10)$$

Where  $\Delta N_i$  is a North shift,  $\Delta E_i$  is a East shift and  $n$  is the number of reference points.

After the computation of the RMSE of all the PRISMA geocoded hyperspectral images, the geolocation accuracy can be computed. As the geolocation accuracy is expressed as the Circular Error at the 90th percentile (CE90) in the PRISMA mission document, the accuracy of the hyperspectral images will also be expressed according to the same expression. The CE90 was computed using the following expression (Pagnutti, 2006; Dolloff and Carr, n.d.):

$$CE90(m) = 1.645 \times \sqrt{\frac{1}{n} \sum_{i=1}^n (\Delta N_i^2) + (\Delta E_i^2)} \quad (6.11)$$

The Circular Error at the 90<sup>th</sup> percentile expresses the positional accuracy of an image, and it defined as the radius of the circle within which 90% of the localisation of a point will fall. In other words, this metric indicates that the location of a point will fall at 90% within the radius of the stated CE90.

A summary of the steps mentioned above can be found in the figure 6.4.

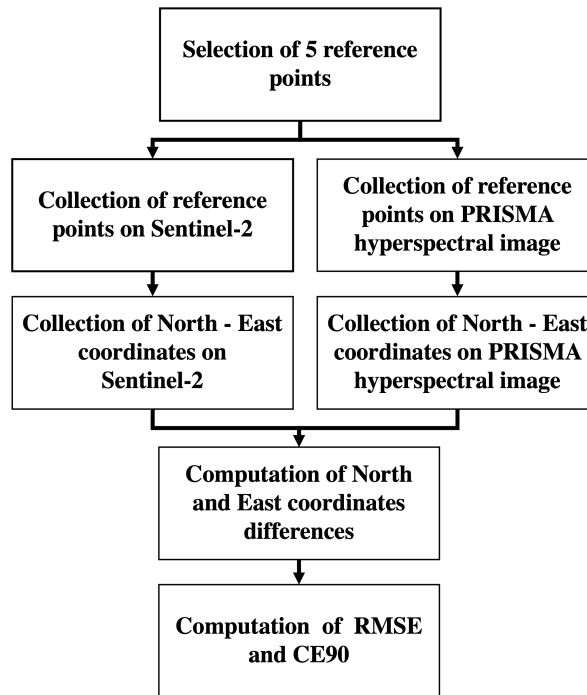


Figure 6.4 – Flowchart of the processing steps to compute the RMSE and CE90.

## 6.3 Orthorectification Process

### 6.3.1 Collection of Ground Control Points

To orthorectify the images according to the proposed methodology, GCPs must be collected manually on each hyperspectral image, which differ from the automatic GCPs matching procedure implemented in the PRISMA products<sup>6</sup>.

In the context of this work, a minimum of four GCPs were collected in each hyperspectral image using the EnMAP- Box plugin available on QGIS. During the collection process, it was ensured that the GCPs are distributed throughout the area delimited by the PRISMA hyperspectral images<sup>7</sup>. To retrieve the necessary image and ground coordinates of the GCPs intended for improving the rational function model, they were marked on both the hyperspectral images and the Sentinel – 2 reference map. Specifically, the hyperspectral images will be used to obtain the image coordinates (row and column), while the ground coordinates (latitude and longitude) will be retrieved from the Sentinel – 2 reference map. Regarding the elevation values of the GCPs, they are retrieved from the 30-meters-resolution Shuttle Radar Topography Mission data.

The table provides the details about the specific GCPs that were collected in each hyperspectral image. In the context of this work, the ground coordinates of the GCPs were acquired in the EPSG:4326 coordinate reference system. The image coordinates (row and column) were retrieved from the L2C hyperspectral images. The location of the different GCPs are provided in the figure 6.5.

ID of Hyperspectral Image	ID of Ground Control Points
1	2,4,5,6,7,8,10,11,12,13,14,16,17,18,20
2	3,6,15,20,22,23
3	1,2,3,4,5,8,9,10,11,13,14,16,18,20
4	2,4,5,6 7,8,11, 14,15,16,17,18,19,20
5	1,3,9,11,12,13,15,16,17,18,19
6	2,3,4,5, 7,9,13,14,17,18
7	2,3,15,19,24

Table 6.2 – List of the ground control points.

The image and ground coordinates of the GCPs of a single hyperspectral image are stored in single CSV file. As a matter of fact, each CSV file has the following data: longitude, latitude, height, column, row and id. The header line of each file must match the format: "Lon, Lat, H, Col, Row, id".

---

6. This matching procedure links image points to corresponding GCPs with exact geolocation with the use of a registration algorithm based on Fourier-Mellin Transformation (ASI, 2021).

7. It is worth noting that the collected points were not the same as the ones used for the assessment of the geolocation accuracy of the geocoded hyperspectral images.

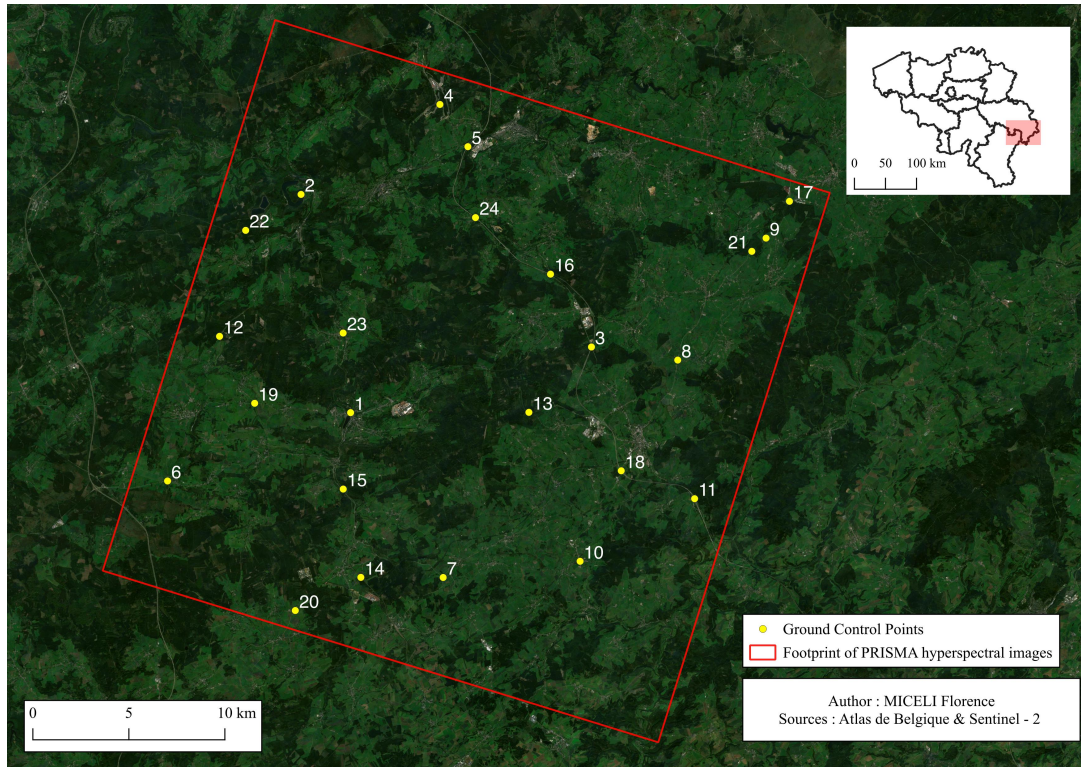


Figure 6.5 – Location of the ground control points.

### 6.3.2 Rational Function Model

Following the collection of GCPs, they are used for the refinement of the RFM. The refinement of the RFM is performed with a Python script that has been especially developed in the scope of this master thesis<sup>8</sup>. The script enables the refinement of the model and the orthorectification of the PRISMA L2C hyperspectral images. The output product is an orthorectified hyperspectral image within the EPSG:4326 coordinate reference system in GeoTIFF format. The images are converted into this format as it is a widely recognized and conventional format for the exchange of geographic data.

The refinement of the RFM involves the following main steps:

1. Assessment of the initial RFM.
2. Refinement of the RFM.
3. Assessment of the refined RFM.

The procedures that will be describe in the following sections are applied to each hyperspectral image separately, indicating independent refinement for every image. In fact, a model will undergo refinement based on the coordinates of GCPs which indicates that the suggested approach involves refining each model individually.

---

<sup>8</sup>. The script has been developed by the promoters of this master thesis. Additionally, the Python script as well as a CSV file and a PRISMA L2C hyperspectral image will be provided on MatheO for to testing the proposed methodology.

### 6.3.2.1 Assessment of the Initial Rational Function Model

The inputs of the Python script are the PRISMA L2C hyperspectral images in HDF5 format and the CSV files containing the image and ground coordinates of the GCPs. To correct one hyperspectral image, both the image itself and the corresponding GCPs file are required. It is worth noting that at least three GCPs must be available to perform this operation.

The first step of the model refinement is the retrieval of the information about this model which are appended to the L2C hyperspectral images. The following information has been retrieved:

- Line, row, latitude, longitude, and height offsets.
- Line, row, latitude, longitude, and height scales.
- Rational polynomial coefficients (RPCs).

Once the relevant information has been obtained, an assessment of the model is performed using the GCPs provided as inputs. The assessment involves determining the difference between the actual image coordinates and the ones estimated with the RFM. Estimated image coordinates are obtained following the computation of the normalized ground coordinates of the GCPs (eq. 6.4, eq. 6.5, eq. 6.6) and the computation of the normalized image coordinates using the provided RPCs (eq. 6.1, eq. 6.2). Following this, the model can be evaluated on the basis of the image coordinate residual errors of the GCPs. The row and column residual errors are computed following the equations 6.12 and 6.13. Afterwards, the mean and the standard deviation of these errors are calculated.

$$\text{Row Residual Error}(RRE) = \text{Observed Row Index} - \text{Computed Row Index} \quad (6.12)$$

$$\text{Column Residual Error}(CRE) = \text{Observed Column Index} - \text{Computed Column Index} \quad (6.13)$$

### 6.3.2.2 Refinement of the Rational Function Model

Once the residual errors have been calculated, the normalized image coordinates are adjusting accordingly to these errors. Then, the RPC are updated to ensure that the polynomials predict the corrected image coordinates. In other words, the coefficients are recalculated based on the adjusted coordinates, so that the polynomials will determine the correct image coordinates. Beyond the GCPs, a DEM is also used during the refinement process. As a result, the rational polynomial coefficients are updated, and the rational function model is refined.

### 6.3.2.3 Assessment of the Refined Rational Function Model

A leave-one-out procedure is conducted to evaluate the effectiveness of the refined model. Also called the leave-one-out cross validation, this procedure is used for the assessment of models. In the context of this work, the leave-one-out validation method consists of selecting one GCP as a test sample, and then computing the RFM with the remaining GCPs. Following this, the selected GCP is used to assess the prediction errors of the computed model with the other GCPs. In other words, the initial model is refined using the training sample and then its predictions errors are evaluated with the test sample. This procedure is iteratively performed until every GCP has been used once as test sample. After computing the prediction errors on the image coordinates of all the GCPs, the mean and standard deviation of these errors are calculated. Thus, the mean and standard deviation of the residual errors on image coordinates of the GCPs are given. During this processing step, it was made sure that the prediction errors do not exceed 2.5 pixels.

If a GCP exceeds this threshold, it is automatically removed and the entire orthorectification process is repeated without the GCP identified as outlier. In the context of this work, all the collected GCPs meet this criterion.

## **6.4 Evaluation of the Hyperspectral Images Orthorectified with the Proposed Methodology**

Upon the completion of the orthorectification process, the reference points that were collected on the PRISMA geocoded hyperspectral images are also collected on the orthorectified hyperspectral images. Considering the same reference points will allow to assess the level of correction as well as the level of geolocation accuracy improvement that can be achieved with the proposed orthorectification process. Following this, the shifts and the related errors can be determined. The geolocation accuracy of the orthorectified hyperspectral images can also be computed. The aforementioned measures can be computed according to earlier presented steps in the figure 6.4.

## **6.5 Assessment of the Orthorectification Process**

Assessing the effectiveness of the proposed methodology for correcting the PRISMA hyperspectral images and enhancing their geolocation accuracy involves a comparison of the shifts and geolocation accuracy before and after the methodology has been applied. Therefore, the differences in the values of the shifts before and after the orthorectification process will be presented. The differences between the geolocation accuracies will also be depicted.

Evaluating the proposed process will provide an indication of its effectiveness to correct the images and improve their geolocation accuracy. It will also enable to know to which extent the methodology can correct and enhance the geolocation accuracy of the PRISMA hyperspectral images.

# Chapter 7

## Results

### 7.1 Manual Collection of the Reference Points and the Ground Control Points

Prior to discussing the results, it is important to note that the reference points and the GCPs were collected manually using the EnMap – Box plugin and the QGIS software. During the collection of these points, some difficulties were faced. Firstly, the identification of the same point locations on both the Sentinel – 2 map and the hyperspectral images was challenging due to the differences in their spatial resolutions. The Sentinel-2 reference map has a 2m spatial resolution, whereas the PRISMA hyperspectral images have a 30m spatial resolution. Moreover, the presence of cloud coverage in some hyperspectral images added difficulties for both the accurate collection of points and the collection of the minimum required number of points. The presence of cloud coverage higher than 10% on hyperspectral images leads to an obscuration of their background and reduces visibility on them, making it difficult to discern details. Furthermore, the clouds and their shadows decrease the collection area of points on these images. Nevertheless, by adjusting the visualisation parameters<sup>1</sup> of these images, it was possible to collect points.

Given the difficulties encountered during the collection of the points, the results presented in the following sections may have been to some extent impacted by inaccuracies. However, the points were collected as accurately as possible in order to limit the potential inaccuracies in these results. Consequently, it is important to consider the impact of the previously mentioned difficulties when interpreting the results.

### 7.2 Evaluation of the PRISMA Geocoded Hyperspectral Images

#### 7.2.1 Detected shifts

The shifts are estimated through the computation of GCPs coordinates difference between the PRISMA geocoded hyperspectral images and the Sentinel – 2 reference map. The shifts detected on each geocoded image is presented in table 7.1.

---

1. Adjusting the visualisation parameters of the images involved to visualise the images in shortwave infrared.

Firstly, it can be observed that the greatest shifts were reported on hyperspectral image 7. In contrast, the hyperspectral image 1 has the smallest shifts. As a matter of fact, it is observed that the image with the greatest cloud coverage percentage has the greatest shifts, while the image with the smallest cloud coverage has the lowest shifts. Considering that the 30m spatial resolution of the PRISMA hyperspectral images, the shifts range between 0.5 pixel to 6 pixels. Furthermore, it can be noted that non-constant shifts have been detected in all PRISMA geocoded hyperspectral images. This suggests that the geolocation accuracy of these images will vary, and that there will be notable differences of the geolocation accuracy between two images acquired over the same area. Furthermore, it can be observed that the North shifts are more important than the East shifts considering all the hyperspectral images.

<b>ID of Hyperspectral Image</b>	<b>East shift (m)</b>	<b>North shift (m)</b>
1	12.5920	46.7764
2	171.5912	118.9626
3	21.6914	41.5566
4	92.2380	107.6369
5	89.2236	118.2865
6	106.1430	119.6149
7	128.1338	107.0038

Table 7.1 – Coordinates shifts of the PRISMA geocoded hyperspectral images.

### 7.2.2 Root Mean Square Errors

The outcomes indicate that the errors range between 14m and 128m on the North coordinate and between 45m and 120m on the East coordinate (table 7.2). Considering that the PRISMA hyperspectral images has a 30m spatial resolution, the errors of the geocoded images are ranging between about 0.5 pixel and 5 pixels on the North coordinate, while errors between 1 pixel and 4 pixels have been observed on the East coordinate. Furthermore, it can be observed that errors are greater on the East coordinate than on the North coordinate. It can also be noted that the geocoded hyperspectral image 2 obtained the highest errors considering both coordinates. This image is followed by the hyperspectral images 7 and 6 which had the second and third highest errors (table 7.2). As a matter of fact, the images with highest percentages of cloud coverage have the highest errors, while the images with cloud coverage close to 0% have the lowest errors. However, it can be noted that the geocoded hyperspectral image which obtained the smallest shifts does not have the smallest errors.

<b>ID of Hyperspectral Image</b>	<b>RMSE - North (m)</b>	<b>RMSE - East (m)</b>
1	14.20461	59.50732
2	172.39410	120.94575
3	22.61114	45.15926
4	94.49388	107.98996
5	89.9113	119.32336
6	108.59911	120.85481
7	128.55604	107.71304

Table 7.2 – Root mean square errors on the North - East coordinates on the PRISMA geocoded hyperspectral images.

### 7.2.3 Geolocation Accuracy

The geolocation accuracy of the PRISMA geocoded hyperspectral images are specified in table 7.9 .

ID of Hyperspectral Image	CE90 (m)
1	100.63975
2	346.41840
3	83.07856
4	236.04991
5	245.77270
6	267.27910
7	275.89330

Table 7.3 – Geolocation accuracy of the PRISMA geocoded hyperspectral images.

The second hyperspectral image has the least accurate geolocation, which was expected since this image obtained the highest shifts and errors on the North and East coordinates. Moreover, hyperspectral images 7 and 6 have the second and third least accurate geolocation, respectively. Although some hyperspectral images have geolocation accuracies lower than 200m, it should be noted that two of the hyperspectral images achieved geolocation accuracy of 100.63975m and 83.07856m. In fact, the hyperspectral images that have the least cloud coverages are the ones that exhibit the highest geolocation accuracies.

## 7.3 Orthorectification

### 7.3.1 Assessment of the Rational Function Models

The initial rational function model is assessed by computing the discrepancies between the observed and computed image coordinates of the GCPs. The GCPs used in the context of the assessment vary depending on the hyperspectral image. Table 7.4 lists details the number of GCPs collected on each hyperspectral image.

ID of Hyperspectral Image	Number of GCPs
1	15
2	6
3	14
4	14
5	11
6	10
7	5

Table 7.4 – Number of GCPs collected on each PRISMA hyperspectral images.

The standard deviation and the mean of row and column residual errors of GCPs are presented in table 7.5. It worth to remind that the residual errors presented in the table may have been affected by the inaccuracies of the image coordinates collected manually on the QGIS software. Nevertheless, the table gives an overview of the performances of the different models to predict the image coordinates of GCPs.

ID of Hyperspectral Image	Standard Deviation (pixel)		Mean (pixel)	
	Row	Column	Row	Column
1	1.010 95	1.130 59	-1.585 98	0.342 59
2	0.958 55	0.692 36	-6.068 87	4.554 69
3	0.740 861	1.053 75	-0.720 47	0.410 48
4	0.967 63	1.057 51	-1.827 25	-2.889 57
5	0.940 16	1.528 34	-2.410 54	-3.300 81
6	0.846 97	0.9996	-2.402 05	-3.479 36
7	0.666 81	1.077 38	-1.381 76	-4.528 49

Table 7.5 – Standard deviation and mean of row and column residual errors of the initial rational function models.

Based on the table 7.5, the mean row residual error values are negative considering all the models. This indicates that the computed row coordinates are underestimated by these models. The highest row residual error was obtained by the rational function model linked to the PRISMA hyperspectral images acquired on 29 June 2020 (ID 2). The mean row residual value is equal to -6.06886 pixels which indicates that the mean row error is about 180m. This observation suggests that the model was unable to accurately estimate the coordinates of the Ground Control Points (GCPs). In addition, this model produced the highest column residual error (table 7.5). It can also be observed that the last four models are underestimating the column coordinate. Furthermore, it can be noted that the column residual errors of six models are higher than 2 pixels meaning their mean error on the column is higher than 60 m.

The standard deviations of the residual errors are ranging between 0.66681 and 1.52833 pixels. Regarding the model with the highest mean residual errors, its standard deviation values suggested that, on average, the residual errors are falling within approximately 1 pixel from the mean row and column residual error. Such observation indicates that significant residual errors have been obtained when assessing the RFM of the hyperspectral image acquired on 29 June 2020. The models linked to the hyperspectral images with the lowest cloud coverage percentages exhibit higher standard deviations which indicates that, on average, residual errors deviate more from the mean residual errors.

Based on the above-mentioned observations, it seems that the model with the greatest residual errors is associated with the hyperspectral image that have the highest cloud coverage percentage. In fact, the second hyperspectral image has the largest cloud coverage percentage (25.06%) and the highest residual errors. Furthermore, the hyperspectral images with the least cloud coverage percentages have the lowest residual errors. Therefore, it seems that the performance of the rational function models might be influenced by the percentage of the cloud coverage.

### 7.3.2 Assessment of the Refined Models

Once the different rational function models have been refined, they are evaluated through a leave-one-out validation process. This process provides a way to estimate the accuracy of the predictions of the different models. The prediction errors of each refined model are available in the appendixes<sup>2</sup>. The residual errors of the refined models are presented in table 7.6.

---

2. The appendixes contain tables that present the row and column errors obtained from the leave-one-out procedure of each refined model

ID of Hyperspectral Image	Standard Deviation (pixel)		Mean (pixel)	
	Row	Column	Row	Column
1	0.554 72	1.255 05	0.022 23	0.050 78
2	1.365 70	1.060 34	0.416 37	-0.183 35
3	0.604 74	0.877 56	-0.056 87	0.052 55
4	0.709 95	1.049 82	-0.023 72	0.050 36
5	0.611 01	1.222 07	0.075 86	0.168 43
6	0.826 09	1.041 80	0.007 65	0.102 99
7	0.451 45	1.488 20	-0.110 50	0.302 97

Table 7.6 – Standard deviation and mean of row and column residual errors of the refined rational function models.

The mean prediction errors over the rows and the columns are less than 1 pixel. Such values indicate that the refined models can achieve accuracy greater than 1 pixel and thereby greater than 30m on both axes. The highest mean prediction errors were obtained with the models using 5 and 6 GCPs during the model refinement process. The model that used 6 GCPs achieved mean prediction errors of 0.41637 and -0.18335 pixels on the row and column axis, respectively. Moreover, the model that used 5 GCPs reached mean prediction errors of -0.11050 and 0.30297 pixels on the same axes. Although these two models are less accurate than the others, they still manage to offer accuracy greater than 1 pixel on both axis. In contrast, the model refined with 15 GPCs achieved mean prediction errors of 0.02223 and 0.05078 pixels for the row and column axis, respectively. Consequently, the accuracy of a refined model on both row and column axes is impacted by the number of control points used during its refinement.

## 7.4 Evaluation of the PRISMA Hyperspectral Images Orthorectified with the Proposed Methodology

### 7.4.1 Detected Shifts

The table 7.7 depicts the shifts in the North - East coordinates detected on the PRISMA hyperspectral images corrected with the suggested approach.

ID of Hyperspectral Image	East shift (m)	North shift (m)
1	21.85040	40.35528
2	20.70880	100.78790
3	27.15920	8.12282
4	14.62280	93.19440
5	20.73986	40.07855
6	19.67300	50.88060
7	51.06880	145.46826

Table 7.7 – Coordinates shifts of the PRISMA hyperspectral images orthorectified with the suggested methodology.

The highest shifts were obtained on the last hyperspectral image and the lowest shifts were obtained on the third hyperspectral image. This image obtained a shift of 27.15920m on the East and a shift of 8.12282m on the North coordinate. Furthermore, it can be observed that the North shifts are greater than the East shifts for all images, with the exception of the third image.

### 7.4.2 Root Mean Square Errors

The outcomes indicate that the errors range between 17m and 56m on the North coordinate and between 11m and 146m on the East coordinate (table 7.8). The hyperspectral image 3 is the image which has the lowest errors considering both North and East coordinates, in contrast to the hyperspectral image 7 obtained the highest errors. Actually, errors of 56.16811m and 146.88992m were obtain on the North and East coordinate, respectively. In addition, there is a difference close 100m between the North -East coordinate errors on this hyperspectral image, which is the highest difference observed between the North - East errors. Furthermore, the errors on the East direction appear to be greater than the North ones.

<b>ID of Hyperspectral Image</b>	<b>RMSE - North (m)</b>	<b>RMSE – EAST (m)</b>
1	25.82730	42.43891
2	32.92046	107.17140
3	27.40884	11.31149
4	17.67571	94.92659
5	25.40891	43.52378
6	27.99757	54.58162
7	56.16811	146.88992

Table 7.8 – Root mean square errors on the North - East coordinates on the PRISMA hyperspectral images orthorectified with the suggested methodology.

### 7.4.3 Geolocation accuracy

The table 7.9 depicts the geolocation accuracy of hyperspectral images orthorectified with the suggested methodology.

<b>ID of Hyperspectral Image</b>	<b>CE90 (m)</b>
1	81.72373
2	184.18092
3	48.77625
4	158.83863
5	82.90428
6	100.90995
7	118.61810

Table 7.9 – Geolocation accuracy of the PRISMA hyperspectral images orthorectified with the suggested methodology.

The third hyperspectral image has the most accurate geolocation, while the second hyperspectral image has the least accurate geolocation. This suggests that the level of geolocation accuracy varies across the different hyperspectral images. Overall, it can be observed that the proposed process has been successful in achieving a geolocation accuracy of less than 200m. However, a CE90 geolocation accuracy of 15 meters has not been achieved despite using GCPs.

# Chapter 8

## Discussion

### 8.1 PRISMA Geocoded Hyperspectral Images

#### 8.1.1 Shifts and Root Mean Square Errors Evaluation

Although there is a limited number of studies that have addressed the shifts in the PRISMA geocoded images, two studies were available, and some comparisons can be made with the identified shifts.

A study reported that a non-constant shift up to 5 pixels has been observed in all PRISMA geocoded images when compared to an ancillary digital cartography of Central and Southern Italy (Mzid *et al.*, 2022). All detected shift in this work are within this limit, except for hyperspectral image 2 which has a shift of approximately 6 pixels. In addition, shifts of varying values were obtained which indicate that the PRISMA geocoded images exhibit a non-constant shift, which is consistent with the findings of the study conducted by Mzid *et al.* (2020).

Furthermore, the shifts identified in the context of this can be evaluated with the studies conducted by Pearlshtien *et al.* (2023). As part of a validation – calibration approach for hyperspectral sensors, the study investigated about the geometric correction performance of the PRISMA satellite. It was reported that shifts were observed between PRISMA geocoded images acquired over the same areas. In fact, a shift of 238.6m in the longitudinal direction and 95.1m in the latitudinal direction were observed between PRISMA images taken in 2019 and 2020 (detected shifts with 200 GCPs coordinates) (Pearlshtien *et al.*, 2023). Based on these results, it can be observed that East shifts are more important than the East shifts. The same observation can be made when comparing two PRISMA geocoded hyperspectral images acquired at different times over Vielsam. As a matter of fact, a shift of 158.9992m in the East direction and a shift of 72.1862m in the North direction were detected between PRISMA images taken in June 2020 (ID2) and April 2020 (ID1). Furthermore, shift of -149.8998m in the East direction and a shift of -77.406m in the North direction were detected between PRISMA images taken in February 2021 (ID3) and June 2020 (ID2) in Vielsam. As a result, the detected shifts are consistent with the outcomes of this study.

According to the aforementioned observations, it can be further noticed that there is a non-shift between the PRISMA geocoded hyperspectral images and that there is a non – constant shift between these images and Sentinel – 2. This indicates that the geometric correction performances of the PRISMA sensor is not consistent and stable which rises questions of the geolocation accuracy of these images.

### 8.1.2 Geolocation accuracy

The computed geolocation accuracies of PRISMA geocoded hyperspectral images revealed that five of them obtained lower accuracies than those specified in the PRISMA Algorithm Theoretical Basis Document (table 7.9). The document states that the CE90 geolocation accuracy of L2 images should be lower than 15m when GCPs are used and lower than 200 m when GCPs are not used. As five images do not meet the declared geolocation accuracies, it can be inferred that the orthorectification process that relies only on the LoS information is not that effective in achieving the levels of geolocation accuracy specified in the PRISMA mission document.

Furthermore, is important to note that the PRISMA geocoded hyperspectral images studied in the context of this work were not orthorectified with GCPs. Initially, it was thought that the GCPs matching procedure was unsuccessful for these images. However, a recent study indicates that the automatic method of GCPs searching has not been carried out yet (Baiocchi *et al.*, 2022). This means that the method is not yet operational, suggesting that the operational level of the PRISMA mission may not be as high as anticipated and that the geolocation accuracy of the current available PRISMA images might not be accurate as the ones specified in the document.

## 8.2 Evaluation of the Refinement Process

To evaluate the effectiveness of of the refinement process with the use of GCPs, a residual error analysis of the refinement modelling can be made. The analysis involves computing the differences between the absolute mean residual errors before and after the refinement process. The outcomes of these differences are displayed in table 8.1 .

ID of Hyperspectral Image	N. of GCPs Used	Mean Row (pixel)	Mean Column (pixel)
1	15	1.56376	0.29181
2	6	5.65249	4.37134
3	14	0.66360	0.35793
4	14	1.80353	2.83921
5	11	2.33468	3.13238
6	10	2.39440	3.37637
7	5	1.27126	4.22552

Table 8.1 – Differences between the absolute mean residual errors before and after the refinement process.

A positive value indicates that the refinement process has led to a reduction in the residual errors whereas a negative value indicates an increase in the residual errors. As a result of this, it can be concluded that refining the models with GCPs reduce the mean residual errors of all the models. Furthermore, the highest reductions are observed within the models which had the highest residual errors. Following the refinement of the model associated to the hyperspectral image 2, decrease of 5.65249 and 4.37135 pixels has been observed for the row and column axes, respectively. As a matter of fact, a decrease of approximately 169.5147m and 131.1405m have been observed, respectively. Such reductions have been possible even though only 6 GCPs were collected (table 8.1). Furthermore, reductions of 1.27126 and 4.22552 pixels were obtained for the model associated to the hyperspectral image 7. Specifically, reductions of 38.1378m and 127.7656m have been obtained. Despite the use of fewer GCPs, the above models were successfully refined and showed the greatest improvement in terms of errors reduction. These outcomes also demonstrate that the proposed methodology is effective in reducing the residual errors, especially for the models with high residual errors.

### 8.3 Evaluation of the Orthorectification Process

The orthorectification technique introduced in this study can be compared with a study that assessed three different orthorectification models for the geometric correction of PRISMA panchromatic images (Baiocchi *et al.*, 2022). The rigorous model<sup>1</sup>, the rational polynomial coefficients model and the rational polynomial functions model were the models investigated for the correction of the PRISMA panchromatic images. The last two models follow the same approach except that polynomial coefficients are provided to the first, while the second estimated them with GCPs. In the context of this work, it was proposed to not use the provided coefficients appended to the PRISMA products but to estimate them with manually collected GCPs. Therefore, an analysis between the rational polynomial function model and the suggested approach can be made. As the proposed approach is close to the Rational Polynomial Function model, a comparison between their results can be made. The maximum accuracy obtained by the rational polynomial function model on three test sites in Central Italy are presented in table 8.2<sup>2</sup>.

N. of polynomial coefficients estimated	N. of GCPs (N. of CP)	East RMSE Value of CP discrepancies (m)	North RMSE Value of CP discrepancies (m)
Rome	6	4.811	4.173
Fucino	6	4.792	5.009
Ischia	5	4.404	4.105

Table 8.2 – Maximum accuracy obtained by the rational polynomial function model on three test sites (Baiocchi *et al.*, 2022).

In the context of this work, none RMSE of such values were obtained. Indeed, the values of the RMSE are twice or fifty times greater than these values. The third hyperspectral image had the lowest RMSE values (27.15920m on the East direction and 8.12282m on the North direction) and the last hyperspectral image has the highest RMSE values (51.06880m on the East direction and 145.46826 on the North direction). However, it should be noted that the results in the study conducted by Baiocchi *et al.* (2022), only 6 coefficients were estimated in contrast to 20 in the context of this work. The study investigated about the potential link between the number of coefficients estimated and the best obtained accuracy. The study reported that the accuracy of the rational polynomial function model decreases as the number of coefficients increases.

---

1. Model defined on the basis of the sensor characteristics Baiocchi *et al.*, 2022).  
2. In the table, "CP" is referred to as CheckPoint)

In particular, it was revealed that the highest accuracy in the East and North coordinates was obtained by estimating only 6 or 5 polynomial coefficients (Baiocchi *et al.*, 2022). As a result of this, the number of computed coefficients could be a potential explanation for the differences observed in the computed accuracy between this work and the study. In the case of the study, 6 or 5 polynomial coefficients were estimated using 6 and 5 GCPs, respectively. In contrast, 20 coefficients were estimated with 4 to 15 GCPs in this work. Based on these findings, it can be inferred that the coefficients were estimated with greater precision in the study compared to this research, resulting in lower RMSE values. As better results are obtained with the methodology proposed, such approach could be interesting. In particular, it was revealed that the highest accuracy in the East and North coordinates was obtained by estimating only 6 or 5 polynomial coefficients (Baiocchi *et al.*, 2022). As a result of this, the number of computed coefficients could be a potential explanation for the differences observed in the computed accuracy between this work and the study. In the case of the study, 6 or 5 polynomial coefficients were estimated using 6 and 5 GCPs, respectively. In contrast, 20 coefficients were estimated with 4 to 15 GCPs in this work. Based on these findings, it can be inferred that the coefficients were estimated with greater precision in the study compared to this research, resulting in lower RMSE values. To achieve a similar level of precision as that described in the study, it would be worthwhile to examine the optimal number of coefficients to be estimated, and to include this in the orthorectification process. With such improvement that suggested methodology could provide more accurate results.

In order to further evaluate the effectiveness of the suggested orthorectification process, the RMSE values obtained from this method can be compared with the the RMSE values obtained from the geometric correction of the EnMAP Level - 1C images. Based on the latest findings from the third EnMAP mission Quarterly Report, The assessment of the geometric accuracy of the EnMAP Level – 1C products is done by matching these images against Sentinel – 2 reference images using matching techniques. Following the matching procedure, checkpoints can be obtained and Mean Deviation as well as RMSE values can be computed (DLR, 2023).

The figure 8.1 depicts the RMSE values of a random sample of 292 Level -1C tiles that have been acquire between 1 January 2023 and 31 March 2023.

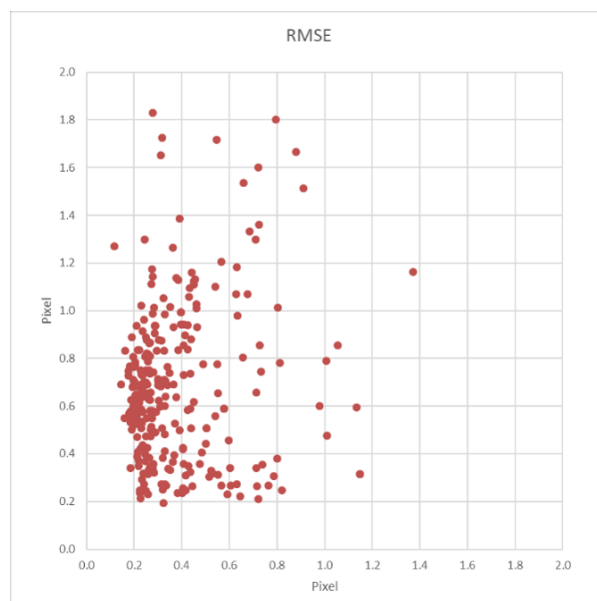


Figure 8.1 – RMSE values for EnMAP L1C products in pixel (DLR, 2023).

The results show that the applied geometric correction lead to RMSE values between 0.15 pixel and 1.4 pixels in the x direction and between 0.2 pixel and 1.85 pixels in the y direction. Considering the 30m spatial resolution of the EnMAP products, it can be said that much lower RMSE values are observed on these data. However, it should be noted that the geometric correction method applied on the EnMAP images is not the same as the one proposed in the context of this word. Following the application of the suggested approach, it was not possible to reach the same results as the ones obtained on EnMAP. In fact, the lowest RMSE value is 17.67571m (0.5 pixels) and the highest RMSE value is 56.16811m (1.5 pixels) considering the North direction. Furthermore, the lowest RMSE value is 11.31149m (0.4pixel) and the highest is 146.88992m (5 pixels) in the East direction. Based on these findings, the proposed correction for the PRISMA hyperspectral images need to be improved.

Even though the suggested methodology do not reach the accuracy obtained in the study conducted by Baiocchi *et al.* (2022) and the accuracy of the EnMAP data, the suggested methodology has been effective to geometrically correct the PRISMA hyperspectral images. Indeed, a decrease of 78.20795m on the North shift and a decrease of 68,48374m in the East shift have been observed following the application of this methodology. Furthermore, a decrease of 68,7343m on the North shift and a decrease of 86.4700m in the East shift have also been observed. The suggested methodology also achieved to decrease the RMSE values in both the North and East direction. Specifically, the methodology allowed a decrease up to 139.47364m in the North direction and a decrease up to 75.79958m in the East direction. Regarding the geolocation accuracy, the applied geometric correction on the PRISMA hyperspectral images has succeeded in enhancing the geolocation accuracy of all hyperspectral images. Specifically, geolocation accuracy improvement between 18m and 166m was achieved. This further indicates the effectiveness of the orthorectification process to improve the geolocation accuracy of these images. However, the computed geolocation accuracies still do not match the stated accuracies of the PRISMA mission document despite the use of GCPs.

## Chapter 9

# Conclusion

The objective of the master thesis was to geometrically correct the PRISMA hyperspectral images for accurate monitoring of changes in photosynthetic activity over forest areas. The proposed methodology for achieving this objective involved an orthorectification process that used ground control points (GCPs).

The approach has been demonstrated to be effective in correcting the PRISMA hyperspectral images. The proposed methodology has resulted in a reduction of errors between these images and the Sentinel – 2 reference map. Specifically, the errors were reduced by up to 139m in the North direction and up to 75m in the East direction. The proposed methodology has also improved the geolocation accuracy of all the hyperspectral images, with the most significant improvement being up to 166m.

However, despite the improvements achieved, the geolocation accuracy of the PRISMA hyperspectral images is still below the accuracy stated in the PRISMA mission document, even with the used of GCPs. Therefore, further improvements are required to obtain higher accurate images. Nevertheless, the developed methodology can serve as a starting point for research aimed at improving the geolocation of the PRISMA hyperspectral images. Furthermore, it can be made available to the scientific community to raise awareness about the geolocation accuracy issue and encourage the development of new methodologies for more accurate correction of these data.

PRISMA hyperspectral data offer a wealth of information that can be used in a wide range of applications. However, the potential use of these data can be limited by the low operational level of the PRISMA mission and the associated issues such as the shift problem, which significantly affects the geolocation accuracy and reliability of the PRISMA hyperspectral images. Although efforts have been made to mitigate this issue, such as the proposed methodology in this work, the problem remains a significant challenge for the accurate mapping and monitoring of forest areas. Therefore, despite the potential benefits offered by PRISMA data, their use is limited by the operational constraints and the related issues linked to the PRISMA mission.

## Chapter 10

# Future Perspectives

Nowadays, there has been an increase in the number of software programs that support the hyperspectral data from the PRISMA mission. The ENVI software has undergone several improvements to enable it to handle PRISMA data format and perform operations on these data. The latest version of the software (5.7 version) contains advanced tools like the RPC orthorectification tool that uses RPC, (x,y,z) coordinates from GCPs and elevation data from a DEM to create an orthorectified image. Further investigation could be done to explore the potential of this tool to correct the PRISMA hyperspectral data. Additionally, the ERDAS IMAGINE, a plugin developed by Planetek Italia, is another program that can be used to explore the potential of PRISMA hyperspectral data. Although licensing constraints prevented the use of the two aforementioned programs, it can still be beneficial to explore what they could offer for processing the PRISMA data. Another software program that can be used to process these data is the EnMAP – Box plugin. Developed in the framework of the imaging spectrometer EnMAP, this plugin allows for spectral analysis and computation of various vegetation indices, but does not enable correction of these data.

Although different software programs support the PRISMA data, given the limitations and the low operational level of the PRISMA mission, it would be more advisable to shift focus towards the use of data from the next-generation hyperspectral missions. The highly anticipated ENMAP hyperspectral mission was launched in April 2022 and will soon deliver its first hyperspectral data. The main objective of this German mission is to provide high quality hyperspectral data at regional scale. Hyperspectral data will be delivered at 30m spatial resolution within the 420 – 2450nm spectral range with a sampling distance of 6.5nm between 420 – 1000nm and 10nm between 900 – 2450nm. Furthermore, the data will be provided with geolocation accuracy of 30m when GCPs will be used and 100m when not used. However, daily assessment of these data revealed that they can achieve geolocation of 55m without GCPs and 20m with GCPs (Storch *et al.*, 2023). Moreover, based on the first results of the mission, the EnMAP hyperspectral data have the potential to be used in various applications. The upcoming FLEX mission could also be very useful in the context of monitoring the photosynthetic activity. The Fluorescence EXplorer satellite is planned to be launched in 2024 and will provide global data about vegetation fluorescence which can be used as an indicator of their photosynthetic activity. The hyperspectral data of this mission will range between the 500 – 780nm spectral with spectral sampling between 0.1nm and 2nm.

The upcoming hyperspectral data of the EnMAP and FLEX missions have the potential to provide valuable information for the monitoring of vegetation photosynthetic activity due to their high spectral resolution and ability to capture data in narrow spectral bands. Specifically, the EnMAP data have the advantage that they would be easily processed using the EnMAP – Box that is already available. However, it is important to acknowledge the limitations of the temporal resolution of these data which might not be sufficient to capture short-term changes in vegetation. To address this limitation, it might be worthwhile to explore the potential of coupling EnMAP data with FLEX data or other sources. This approach could potentially provide a more complete and accurate picture of photosynthetic activity, and thereby helping to better understand the impacts of climate change on ecosystem health and developing more effective management strategies for mitigating its effects.

# Chapter 11

## Appendixes

### 11.1 Appendix 1

The Python scripts developed in the context of this master thesis are available on the MatheO website. The following scripts are available:

- `init.py`
- `cly.py`
- `main.py`
- `PRISMAtoolbox.py`
- `rpcmodel.py`

A data sample is available for testing the scripts, which includes:

- CSV file containing the coordinates of GCPs.
- Digital Elevation Model.
- PRISMA hyperspectral image at Level -2

In order to execute the scripts, it is necessary to adjust the folder path names and file names.

## 11.2 Appendix 2

Test sample (GCP ID)	Column error (pixel) 2	Row error (pixel)	Mod (pixel)
2	1.081096	-0.168947	1.094218
4	-1.789248	-1.457879	2.307990
5	-1.512844	1.089821	1.864512
6	1.022396	0.108633	1.028151
7	-1.310496	-0.220952	1.328992
8	0.259111	-0.021257	0.259982
10	-0.115862	-0.211827	0.241443
11	1.444022	-0.115041	1.448597
12	2.156272	0.396431	2.192411
13	-0.897068	-0.066208	0.899508
14	-0.895378	0.011616	0.895453
16	-0.531428	-0.158178	0.554469
17	1.950436	0.672969	2.063271
18	-0.328781	0.010579	0.328951
20	0.229475	0.463633	0.517315

RFM model prediction errors for the GCPs collected on the hyperspectral image acquired on 20 April 2020 (ID 1).

## 11.3 Appendix 3

Test sample (GCP ID)	Column error (pixel)	Row error (pixel)	Mod (pixel)
3	-0.564513	1.974684	2.053790
6	0.057439	0.277238	0.283126
15	1.552222	-1.758747	2.345759
20	-1.613982	1.676205	2.326929
22	0.150245	-0.300746	0.336187
23	-0.681501	0.629602	0.927816

RFM model prediction errors for the GCPs collected on the hyperspectral image acquired on 29 June 2020 (ID 2).

## 11.4 Appendix 4

Test sample (GCP ID)	Column error (pixel)	Row error (pixel)	Mod (pixel)
1	0.056845	0.425770	0.429548
2	2.176358	-0.110503	2.179162
3	-1.150743	0.281213	1.184606
4	-0.550629	-0.448692	0.710293
5	-0.402386	0.834291	0.926259
8	-0.283592	0.272270	0.393135
9	0.771722	-1.373610	1.575550
10	0.195624	0.010593	0.195910
11	1.311199	0.659474	1.467702
13	-0.722968	-0.541172	0.903078
14	-0.614089	-0.911621	1.099162
16	-0.369701	0.239447	0.440470
18	0.173453	-0.214093	0.275539
20	0.144552	0.080489	0.165450

RFM model prediction errors for the GCPs collected on the hyperspectral image acquired on 27 February 2021 (ID 3).

## 11.5 Appendix 5

Test sample (GCP ID)	Column error (pixel)	Row error (pixel)	Mod (pixel)
2	1.275703	-0.105322	1.280043
4	-0.433980	-1.006021	1.095635
5	-1.491578	1.439660	2.073023
6	1.855320	-1.127515	2.171061
7	-0.796591	-0.160923	0.812683
8	-0.130231	-0.171097	0.215022
11	1.212782	0.298396	1.248952
14	-0.565388	-0.096073	0.573492
15	-0.330193	-0.583140	0.670135
16	-1.239205	0.470001	1.325342
17	1.445976	-0.626183	1.575738
18	0.067646	-0.092836	0.114867
19	0.502411	0.545505	0.741615
20	-0.667622	0.883454	1.107344

RFM model prediction errors for the GCPs collected on the hyperspectral image acquired on 15 April 2022 (ID 4).

## 11.6 Appendix 6

Test sample (GCP ID)	Column error (pixel)	Row error (pixel)	Mod (pixel)
1	-1.308401	-0.572817	1.428297
3	-1.637295	0.171478	1.646250
9	1.045115	0.572116	1.191462
11	0.987378	1.114387	1.488883
12	1.664595	0.711849	1.810416
13	-1.102778	-0.397182	1.172123
15	0.379227	0.120460	0.397900
16	-1.216404	-0.749139	1.428583
17	0.962814	-0.039744	0.963634
18	0.827836	-0.606819	1.026421
19	1.250625	0.509837	1.350554

RFM model prediction errors for the GCPs collected on the hyperspectral image acquired on 5 July 2022 (ID 5).

## 11.7 Appendix 7

Test sample (GCP ID)	Column error (pixel)	Row error (pixel)	Mod (pixel)
2	1.994395	-0.388221	2.031828
3	-0.980544	0.380787	1.051887
4	-0.920411	-1.367320	1.648248
5	-0.966858	1.540689	1.818939
7	-0.391234	0.231000	0.454340
9	0.544819	-0.840603	1.001720
13	-0.396932	0.054598	0.400669
14	0.985425	-0.206935	1.006918
17	1.251593	0.870809	1.524728
18	-0.090398	-0.198262	0.217898

RFM model prediction errors for the GCPs collected on the hyperspectral image acquired on 30 September 2022 (ID 6).

## 11.8 Appendix 8

Test sample (GCP ID)	Column error (pixel)	Row error (pixel)	Mod (pixel)
2	1.228701	-0.374355	1.284464
3	2.230620	-0.737250	2.349298
15	-0.892867	0.184291	0.911688
19	0.335134	-0.022827	0.335911
24	-1.386738	0.397650	1.442625

RFM model prediction errors for the GCPs collected on the hyperspectral image acquired on 10 November 2022 (ID 7).

# Bibliography

- [1] Amici, S., & Piscini, A. (2021). Exploring PRISMA Scene for Fire Detection: Case Study of 2019 Bushfires in Ben Halls Gap National Park, NSW, Australia. *Remote Sensing*, 13(8), Article 8. <https://doi.org/10.3390/rs13081410>.
- [2] Angelopoulou, T., Chabrillat, S., Pignatti, S., Milewski, R., Karyotis, K., Brell, M., Ruhtz, T., Bochtis, D., & Zalidis, G. (2023). Evaluation of Airborne HySpex and Spaceborne PRISMA Hyperspectral Remote Sensing Data for Soil Organic Matter and Carbonates Estimation. *Remote Sensing*, 15(4), Article 4. <https://doi.org/10.3390/rs15041106>.
- [3] ASI. (2009). *The PRISMA mission*. [Informative Note]. ASI, Italy. <https://www.asi.it/wp-content/uploads/2020/03/The-PRISMA-mission.pdf>
- [4] ASI. (2020). *PRISMA Products Specification Document Issue 2.3*. [https://prisma.asi.it/missionselect/docs/PRISMA%20Product%20Specifications\\_Is2\\_3.pdf](https://prisma.asi.it/missionselect/docs/PRISMA%20Product%20Specifications_Is2_3.pdf)
- [5] ASI. (2021). PRISMA Algorithm Theoretical Basis Document (ATBD). [http://prisma.asi.it/missionselect/docs/PRISMA%20ATBD\\_v1.pdf](http://prisma.asi.it/missionselect/docs/PRISMA%20ATBD_v1.pdf)
- [6] Baiocchi, V., Giannone, F., & Monti, F. (2022). How to Orient and Orthorectify PRISMA Images and Related Issues. *Remote Sensing*, 14(9), Article 9. <https://doi.org/10.3390/rs14091991>
- [7] Bonis, R. D., & Laneve, G. (2014). Development of a vegetation damage severity index for the Italian hyperspectral sensor PRISMA.
- [8] Bresciani, M., Giardino, C., Fabbretto, A., Pellegrino, A., Mangano, S., Free, G., & Pinardi, M. (2022). Application of New Hyperspectral Sensors in the Remote Sensing of Aquatic Ecosystem Health: Exploiting PRISMA and DESIS for Four Italian Lakes. *Resources*, 11(2), Article 2. <https://doi.org/10.3390/resources11020008>
- [9] Chou, S., Chen, J. M., Yu, H., Chen, B., Zhang, X., Croft, H., Khalid, S., Li, M., & Shi, Q. (2017). Canopy-Level Photochemical Reflectance Index from Hyperspectral Remote Sensing and Leaf-Level Non-Photochemical Quenching as Early Indicators of Water Stress in Maize. *Remote Sensing*, 9(8), Article 8. <https://doi.org/10.3390/rs9080794>
- [10] Chu, S., Hust, G. S., Graybeal, J. D., & Stoner, J. O. (2023, March 11). *Spectroscopy / Definition, Types, & Facts | Britannica*. Britannica.Com. <https://www.britannica.com/science/spectroscopy>. Viewed on 20 March 2023.
- [11] DLR.(n.d.). EnMAP - Mission. <https://www.enmap.org/mission>. Viewed on 15 June 2023.
- [12] DLR. (2023). EnMAP Ground Segment—Mission Quarterly Report 3.
- [13] Eismann, M. T. (2012). *Hyperspectral Remote Sensing*. SPIE. <https://doi.org/10.1117/3.899758>

- [14] ESA. (2012). PRISMA (Hyperspectral). EoPortal. <https://www.eoportal.org/satellite-missions/prisma-hyperspectral#hsis-users-opportunity>. Viewed on February 2023.
- [15] ESA. (2017). *FLEX (Fluorescence Explorer)*. <https://www.eoportal.org/satellite-missions/flex#eop-quick-facts-section>. Viewed on 11 August 2023.
- [16] ESA. (2020). *Chime (Copernicus Hyperspectral Imaging Mission for the Environment)*. EoPortal. <https://www.eoportal.org/satellite-missions/chime-copernicus#eop-quick-facts-section>. Viewed on March 2023.
- [17] Feingersh, T., & Dor, E. B. (2015). SHALOM – A Commercial Hyperspectral Space Mission. In *Optical Payloads for Space Missions* (pp. 247–263). John Wiley & Sons, Ltd. <https://doi.org/10.1002/9781118945179.ch11>
- [18] Gamon, J. A., Peñuelas, J., & Field, C. B. (1992). A narrow-waveband spectral index that tracks diurnal changes in photosynthetic efficiency. *Remote Sensing of Environment*, 41(1), 35–44. [https://doi.org/10.1016/0034-4257\(92\)90059-S](https://doi.org/10.1016/0034-4257(92)90059-S)
- [19] Garbulsky, M. F., Peñuelas, J., Gamon, J., Inoue, Y., & Filella, I. (2011). The photochemical reflectance index (PRI) and the remote sensing of leaf, canopy and ecosystem radiation use efficiencies: A review and meta-analysis. *Remote Sensing of Environment*, 115(2), 281–297. <https://doi.org/10.1016/j.rse.2010.08.023>
- [20] Garini, Y., Young, I. T., & McNamara, G. (2006). Spectral imaging: Principles and applications. *Cytometry Part A*, 69A(8), 735–747. <https://doi.org/10.1002/cyto.a.20311>
- [21] Giardino, C., Bresciani, M., Braga, F., Fabbretto, A., Ghirardi, N., Pepe, M., Gianinetto, M., Colombo, R., Cogliati, S., Ghebrehiwot, S., Laanen, M., Peters, S., Schroeder, T., Concha, J. A., & Brando, V. E. (2020). First Evaluation of PRISMA Level 1 Data for Water Applications. *Sensors*, 20(16), Article 16. <https://doi.org/10.3390/s20164553>
- [22] Guarini, R., Loizzo, R., Facchinetti, C., Longo, F., Ponticelli, B., Faraci, M., Dami, M., Cosi, M., Amoruso, L., Pasquale, V., Nicolo, T., Santoro, F., Colandrea, P., Miotti, E., & Di Nicolantonio, W. (2018). *Prisma Hyperspectral Mission Products*. 179–182. <https://doi.org/10.1109/IGARSS.2018.8517785>
- [23] Hamzeh, S., Hajeb, M., Alavi Panah, S. K., & Verrelst, J. (2023). RETRIEVAL OF SUGARCANE LEAF AREA INDEX FROM PRISMA HYPERSPECTRAL DATA. *ISPRS Annals of the Photogrammetry, Remote Sensing and Spatial Information Sciences*, X-4/W1-2022, 271–277. <https://doi.org/10.5194/isprs-annals-X-4-W1-2022-271-2023>
- [24] *Imaging Spectroscopy: Concept, Approach, Calibration, Atmospheric Compensation, Research and Applications*. (n.d.). Aviris.Jpl.Nasa.Gov. <https://aviris.jpl.nasa.gov/html/aviris.spectroscopy.html>. Viewed on April 2023.
- [25] Japan Space Systems. (n.d.). **HISUISatellite System and Earth Observation-Japan Space Systems**. HISUISatellite System and Earth ObservationJapan Space Systems.<https://www.jspacesystems.or.jp/en/project/observation/hisui/>. Viewed on April 2023.
- [26] Kokhanovsky, A., Di Mauro, B., & Colombo, R. (2022). Snow surface properties derived from PRISMA satellite data over the Nansen Ice Shelf (East Antarctica). *Frontiers in Environmental Science*, 10. <https://www.frontiersin.org/articles/10.3389/fenvs.2022.904585>

- [27] Landsat 1. (2021). <https://landsat.gsfc.nasa.gov/satellites/landsat-1/>. Viewed on March 2023.
- [28] Loizzo, R., Ananasso, C., Guarini, R., Lopinto, E., Candela, L., & Pisani, A. R. (2016, May 1). *THE PRISMA HYPERSPECTRAL MISSION*.
- [29] Lopinto, E., & Ananasso, C. (2013). *The Prisma Hyperspectral Mission*.
- [30] Mulero, G., Jiang, D., Bonfil, D. J., & Helman, D. (2023). Use of thermal imaging and the photochemical reflectance index (PRI) to detect wheat response to elevated CO<sub>2</sub> and drought. *Plant, Cell & Environment*, 46(1), 76–92. <https://doi.org/10.1111/pce.14472>
- [31] Mzid, N., Castaldi, F., Tolomio, M., Pascucci, S., Casa, R., & Pignatti, S. (2022). Evaluation of Agricultural Bare Soil Properties Retrieval from Landsat 8, Sentinel-2 and PRISMA Satellite Data. *Remote Sensing*, 14(3), Article 3. <https://doi.org/10.3390/rs14030714>
- [32] Nesme, N., Marion, R., Lezeaux, O., Doz, S., Camy-Peyret, C., & Foucher, P.-Y. (2021). Joint Use of in-Scene Background Radiance Estimation and Optimal Estimation Methods for Quantifying Methane Emissions Using PRISMA Hyperspectral Satellite Data: Application to the Korpezhe Industrial Site. *Remote Sensing*, 13(24), Article 24. <https://doi.org/10.3390/rs13244992>
- [33] Nuttle, W. (2021). Ecohydrology Defined. The Shadow. <https://medium.com/the-shadow/ecohydrology-defined-2ee09c0d2020>. Viewed on June 2023
- [34] Ortenberg, F. (2011). *Hyperspectral Sensor Characteristics*(pp. 39–68). <https://doi.org/10.1201/b11222-5>
- [35] Orthorectification. (n.d.). GIS Dictionary. <https://support.esri.com/en-us/gis-dictionary/orthorectification>. Viewed on April 2023.
- [36] Pagnutti, M. (2006). *Measurement Sets and Sites Commonly Used for High Spatial Resolution Image Product Characterization*.
- [37] Pearlshtien, D. H., Pignatti, S., & Ben-Dor, E. (2023). Vicarious CAL/VAL Approach for Orbital Hyperspectral Sensors Using Multiple Sites. *Remote Sensing*, 15(3), Article 3. <https://doi.org/10.3390/rs15030771>
- [38] Pepe, M., Pompilio, L., Gioli, B., Busetto, L., & Boschetti, M. (2020). Detection and Classification of Non-Photosynthetic Vegetation from PRISMA Hyperspectral Data in Croplands. *Remote Sensing*, 12(23), Article 23. <https://doi.org/10.3390/rs12233903>
- [39] Pignatti, S., Amodeo, A., Carfora, M. F., Casa, R., Mona, L., Palombo, A., Pascucci, S., Rosoldi, M., Santini, F., Laneve, G. (2022). PRISMA L1 and L2 Performances within the PRISCAV Project: The Pignola Test Site in Southern Italy. *Remote Sensing*, 14(9), Article 9. <https://doi.org/10.3390/rs14091985>
- [40] Pu, R. (2017). *Hyperspectral Remote Sensing: Fundamentals and Practices*. CRC Press. [://doi.org/10.1201/9781315120607](https://doi.org/10.1201/9781315120607)
- [41] Qian, S.-E. (2021). Hyperspectral Satellites, Evolution, and Development History. *IEEE Journal of Selected Topics in Applied Earth Observations and Remote Sensing*, 14, 7032–7056. <https://doi.org/10.1109/JSTARS.2021.3090256>
- [42] Root Mean Square Error (RMSE). (n.d.). C3 AI. <https://c3.ai/glossary/data-science/root-mean-square-error-rmse/>. Viewed on July 2023.

- [43] Romaniello, V., Silvestri, M., Buongiorno, M. F., & Musacchio, M. (2020). Comparison of PRISMA Data with Model Simulations, Hyperion Reflectance and Field Spectrometer Measurements on ‘Piano delle Concazze’ (Mt. Etna, Italy). *Sensors*, 20(24), Article 24. <https://doi.org/10.3390/s20247224>
- [44] The ICOS station network. (n.d.). ICOS. <https://www.icos-cp.eu/observations/station-network>. Viewed on October 2022
- [45] Tuzcu Kokal, A., İsmailoğlu, İ., & Musaoğlu, N. (2022). COMPARISON OF LANDSAT-9 AND PRISMA SATELLITE DATA FOR LAND USE / LAND COVER CLASSIFICATION. *The International Archives of the Photogrammetry, Remote Sensing and Spatial Information Sciences*, XLVI-M-2-2022, 197–201. <https://doi.org/10.5194/isprs-archives-XLVI-M-2-2022-197-2022>
- [46] Vangi, E., D’Amico, G., Francini, S., Giannetti, F., Lasserre, B., Marchetti, M., & Chirici, G. (2021). The New Hyperspectral Satellite PRISMA: Imagery for Forest Types Discrimination. *Sensors*, 21(4), Article 4. <https://doi.org/10.3390/s21041182>
- [47] Yang, J. C., Magney, T. S., Yan, D., Knowles, J. F., Smith, W. K., Scott, R. L., & Barron-Gafford, G. A. (2020). The Photochemical Reflectance Index (PRI) Captures the Ecohydrologic Sensitivity of a Semiarid Mixed Conifer Forest. *Journal of Geophysical Research: Biogeosciences*, 125(11), e2019JG005624. <https://doi.org/10.1029/2019JG005624>
- [48] Zhang, C., Filella, I., Liu, D., Ogaya, R., Llusià, J., Asensio, D., & Peñuelas, J. (2017). Photochemical Reflectance Index (PRI) for Detecting Responses of Diurnal and Seasonal Photosynthetic Activity to Experimental Drought and Warming in a Mediterranean Shrubland. *Remote Sensing*, 9(11), Article 11. <https://doi.org/10.3390/rs9111189>
- [49] Zhou, G., Li, X., Yue, T., Huang, W., He, C., & Huang, Y. (2018). SOLVING THE RATIONAL POLYNOMIAL COEFFICIENTS BASED ON L CURVE. *The International Archives of the Photogrammetry, Remote Sensing and Spatial Information Sciences*, XLII-3, 2511–2515. <https://doi.org/10.5194/isprs-archives-XLII-3-2511-2018>
- [50] Zulfqar, S., Sharif, S., Saeed, M., & Tahir, A. (2021). Role of Carotenoids in Photosynthesis. In M. Zia-Ul-Haq, S. Dewanjee, & M. Riaz (Eds.), *Carotenoids: Structure and Function in the Human Body* (pp. 147–187). Springer International Publishing. <https://doi.org/10.1007/978-3-030-46459-2-5>